



Stability, Failure and Design of I-Section Steel Beams Subjected to Tension

João Tomás¹, Joanna Nseir², Dinar Camotim¹, Nicolas Boissonnade²

Abstract

This paper reports the results of an analytical, numerical and experimental investigation dealing with I-section steel members acted by a combination of major-axis bending and axial (“beams subjected to tension”), which is relatively rare in practice and, therefore, has received little attention in the past. In particular, there are no guidelines for the design against buckling ultimate limit states of such members (only their cross-section resistance is checked). This means that the axial tension favorable effect on lateral-torsional buckling/failure is neglected, leading to over-conservative designs – indeed, a beam subjected to axial tension is currently designed against lateral-torsional failure as a “pure beam”. In order to acquire scientific knowledge and provide design guidance on this topic, the lateral-torsional stability, failure and design of hot-rolled steel I-beams with fork-type end supports and acted by simple transverse loadings (mostly applied end moments) and various axial tension values are addressed in this work. After developing and validating an analytical expression to calculate critical buckling moments of beams under uniform bending and axial tension, beam finite element buckling results are presented for the non-uniform bending cases. Then, two full-scale tests involving a narrow and a wide flange beam under eccentric tension are described and their results are used to develop finite element models, subsequently employed to perform a parametric study aimed at gathering a fairly extensive ultimate strength/moment data bank. Finally, this data bank is used to assess the merits of a design approach proposed here for beams subjected to tension and collapsing in lateral-torsional modes – this design approach, which consists of slightly modifying the current procedure prescribed in Eurocode 3 to design beams against lateral-torsional failures, is shown to provide ultimate moment estimates that correlate very well with the values obtained from the numerical simulations.

1. Introduction

In recent years, the technical and scientific community dealing with steel structures has devoted a considerable effort to the development of efficient (safe and economic) procedures and formulae (interaction equations) for the design and safety checking of steel members (i) subjected to different combinations of internal forces and moments and (ii) susceptible to global instability phenomena, namely flexural buckling (members under compression) and/or lateral-torsional buckling (open-section members under major-axis bending). Moreover, the vast majority of the existing studies concern I-section members, by far the most widely used in the steel construction industry. This fact is reflected in the very large number of “fine-tuned” expressions (interaction equations), intended for the design and safety checking of I-section members, appearing in the current steel design codes. For instance, the latest version of

¹ Civil Engineering Department, ICIST, Instituto Superior Técnico, Technical University of Lisbon, Portugal.

² Civil Engineering Department, University of Applied Sciences of Western Switzerland (Fribourg), Switzerland.

Eurocode 3 (CEN 2005) contains a plethora of rather elaborate (and also fairly complex) formulae and equations aimed at the design of narrow-flange (I) and wide-flange (H) cross-sections and members subjected to arbitrary internal forces and moment diagrams – the interested reader can find the background of most of these formulae and equations in the ECCS (European Convention for Constructional Steelwork) report stemming from the activity of its Technical Committee on Stability (TC8) and co-authored by Boissonnade *et al.* (2006).

However, quite surprisingly (in view of what was mentioned in the previous paragraph), virtually no information can currently be found concerning the structural response and design of I-section members subjected to major-axis bending and tension (*i.e.*, beams under tension), namely on how the presence of tension affects (improves) the beam lateral-torsional buckling behavior. Indeed, the rather complete literature search carried out by the authors bore no fruits and, moreover, no information was obtained from several world-wide recognized experts on lateral-torsional buckling that were contacted very recently. The sole exception to the above situation is the previous (pre-norm) version of Eurocode 3 (CEN 1992), which included provisions concerning the safety checking of beams under tension. Such provisions, whose existence provided the motivation for the study reported in this work, are based on an “effective (reduced) bending moment” concept – however, once more, no trace of background information concerning these provisions could be found. Of course, part of the explanation for the “information void” on this problem is due to the fact that (i) beams under tension occur seldom in practice and (ii) neglecting the tension effects leads to conservative ultimate strength estimates against lateral-torsional failures (the member is designed or safety checked as a “pure beam”). Nevertheless, it is important to investigate the behavior, collapse and design of beams susceptible to lateral-torsional buckling and subjected to tension, namely to acquire information on how conservative are the ultimate strength predictions that neglect the tension effects. The objective of this paper is precisely to contribute to such an investigation, by bridging the lack of scientific information and technical guidance concerning the lateral-torsional stability, behavior/failure and design of beams under tension. It deals specifically with (doubly symmetric) hot-rolled steel I-section beams exhibiting “fork-type” end supports and subjected to simple transverse loadings (*e.g.*, applied end moments) and not affected by local buckling phenomena – beams with a compact cross-section (class 1 or 2 cross-section, according to the Eurocode 3 nomenclature) that can reach its plastic resistance.

Initially, the paper presents the derivation and validation, through the comparison with beam finite element results, of an analytical expression that provides critical buckling moments associated with the lateral-torsional stability (bifurcation) of uniformly bent beams subjected to tension. Then, the analytical study is (numerically) extended to beams under non-uniform bending (mostly stemming from unequal applied end moments) – several beam finite element results concerning the beneficial influence of axial tension on the lateral-torsional stability are presented and discussed in some detail. Next, the paper describes the experimental set-up, procedure and obtained results concerning two full-scale tests, involving a narrow and a wide flange beam subjected to eccentric axial tension, that were performed (i) to acquire in-depth knowledge about the problem under consideration and (ii) to provide the means to develop and validate beam and shell finite element models, in the software FINELG (2012), to subsequently perform an extensive parametric study. This parametric study, carried out in order to assemble a fairly large ultimate strength/moment data bank, involves more than 2000 numerical simulations concerning beams with various cross-section shapes, lengths, yield stresses, acting bending moment diagrams and axial tension levels. This data bank is then used to assess the merits of a design approach proposed in this work for beams subjected to tension and collapsing in lateral-torsional modes – this design approach, which consists of a

slight modification of the current procedure prescribed in Eurocode 3 to design beams against lateral-torsional failures, is shown to provide ultimate moment estimates that correlate very well with the values obtained from the FINELG numerical simulations.

2. Lateral Torsional Stability

This section addresses the influence of tension on the lateral-torsional stability/buckling behavior of simply supported (“fork-type” supports – free warping and flexural rotations) doubly-symmetric I-section beams subjected to major-axis bending – *i.e.*, to assess how the presence of an axial tension N_t changes/increases the critical buckling moment M_{cr} . Of course, it is assumed that N_t is such that the beam cross-section resistance (under bending moment and axial force) is not reached prior to the occurrence instability (bifurcation) – otherwise, if N_t is large enough, the beam collapse stems exclusively from plasticity effects. The first step consists of the analytical derivation and numerical validation, through ABAQUS beam finite element analyses (BFEA), of an expression providing critical moments of uniformly bent beams acted by tension. Next, a numerical investigation, again carried out by means of ABAQUS BFEA and aimed at assessing the effect of tension on the critical moment of beams acted by several non-uniform bending diagrams, is presented and discussed.

2.1 Beams under Uniform Bending – Analytical Study

Consider the beam depicted in Fig. 1(a), which is subjected to uniform major-axis bending (M_y) and tension (N_t) – x is the longitudinal axis and the y and z are the cross-section major and minor centroidal axes. Fig. 1(b) shows the beam adjacent equilibrium configuration associated with the occurrence of lateral-torsional buckling – the deformed configuration axes ζ - η - ξ correspond to their initial (undeformed) counterparts x - y - z .

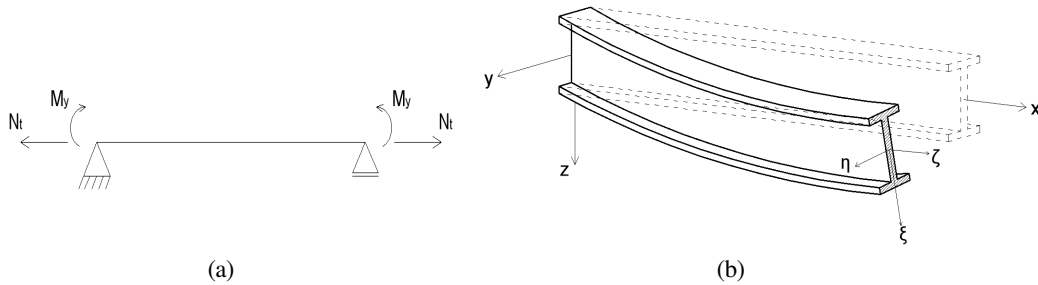


Figure 1: Beam subjected to major-axis bending M_y and axial tension N_t ; (a) general view and (b) deformed configuration associated with the occurrence of lateral torsional buckling

Following the derivations presented in the classical monographs by Chen & Atsuta (1977) and Trahair (1993) for the lateral-torsional stability of beam-columns (*i.e.*, members under major-axis bending and axial compression), the equations ensuring adjacent equilibrium for members subjected to major-axis bending and axial tension read (note the change in sign of the N_t terms and recall that pre-buckling deformations are neglected)

$$EI_z v^{IV} + N_t v'' + M_y \phi'' = 0 \quad (1)$$

$$EI_w \phi^{IV} - (GI_t + N_t r_0^2) \phi'' + M_y v'' = 0 \quad (2)$$

where v and ϕ are the minor-axis bending displacements and torsional rotations, respectively. In order to obtain the critical buckling moment, it is necessary to solve the eigenfunction problem defined by Eqs. (1) and (2). Following the approach adopted by Culver (1966) to obtain analytical solution for beam-columns subjected to bending, it can be shown that the beam buckling mode is expressed by the sinusoidal functions

$$v(x) = A_1 \sin(\pi/L x) \quad (3)$$

$$\phi(x) = A_2 \sin(\pi/L x) \quad (4)$$

satisfying all the problem boundary conditions, it is possible to obtain the expression

$$M_{cr}(N_t) = \sqrt{\left(1 + \frac{N_t}{P_{e,z}}\right)\left(1 + \frac{N_t}{P_{e,t}}\right)} M_{cr}(0) \quad (5)$$

which provides the critical buckling moment of a member subjected to bending and tension. In this expression, (i) $M_{cr}(0)$ denotes the critical buckling moment of the “pure beam” (member under uniform bending only), and (ii) $P_{cr,z}$ and $P_{cr,\phi}$ are given by

$$P_{cr,z} = \frac{\pi^2 E I_z}{L^2} \quad (6)$$

$$P_{cr,\phi} = \left(\frac{\pi^2 E I_w}{L^2} + G I_t\right) \frac{1}{r_0^2} \quad (7)$$

and their values correspond to the symmetric of the minor-axis flexural and torsion buckling loads of the “pure column” (member under uniform compression only). Eq. (5) confirms (and quantifies, for the particular case under consideration) the beneficial effect of tension on the member lateral-torsional buckling moment – *i.e.*, the additional bending and torsional stiffness values, stemming from the presence of N_t , lead to a M_{cr} increase.

In order to provide validation for the derived analytical expression, Fig. 2 depicts the variation of the critical buckling moment increase $[M_{cr}(N_t)/M_{cr}(0)]$ with the ratio N_t/M_y , for an IPE300 beam with length $L=10m$ – the results shown are obtained with Eq. (5) (solid line) and ABAQUS BFE buckling analyses (dashed line). It is observed that (i) there is a virtually perfect agreement between the analytical and numerical values, and (ii) the critical moment increase grows exponentially with applied tension level – for N_t/M_y larger than 9.6, lateral-torsional buckling no longer occurs (the whole beam is under tension).

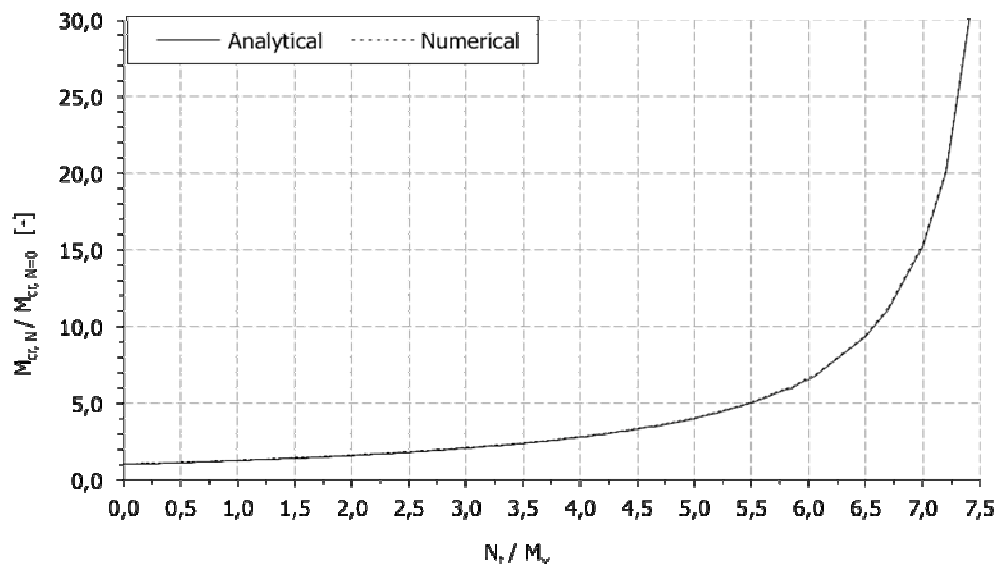


Figure 2: Variation of the critical buckling moment increase $M_{cr}(N_t)/M_{cr}(0)$ with N_t (IPE 300 + $L=10m$)

2.2 Beams under Non-Uniform Bending – Numerical Investigation

ABAQUS BFEA analyses are employed to determine the critical buckling moments of beams (i) built from four hot-rolled profiles (IPE300, IPE500, HEB300, HEB500), (ii) with lengths comprised between 0.5 and 25 m, (iii) subjected to the bending moment diagrams stemming from the loadings depicted in Fig. 3 (unequal end moments or uniformly distributed load applied along the centroid/shear centre axis) and (iv) acted by tension values such that $\beta=N_t/M_y=0; 0.5; 0.75; 1.0; 1.5; 2.0$ (M_y is the maximum applied bending moment) – the transverse and axial loads are applied proportionally.

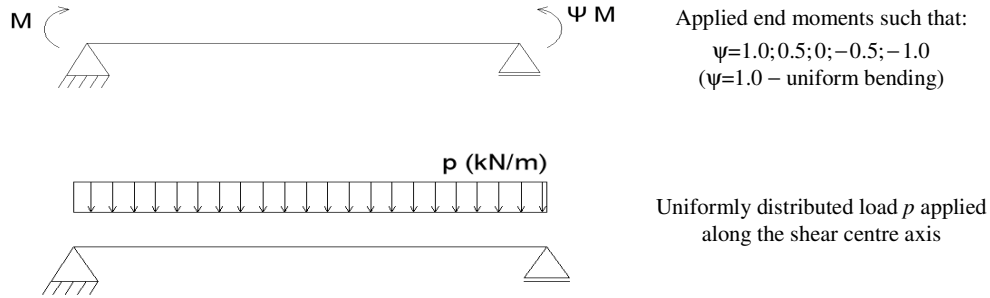


Figure 3: Transverse loadings considered in the numerical lateral-torsional buckling analyses.

Due to space limitations, only a representative sample of the numerical critical buckling moments obtained is presented in this work – the interested reader can find the full set of results (qualitatively similar to those displayed here) in Tomás (2013). Fig. 4 concerns IPE300 beams subjected to the bending moment diagram associated with $\psi=0$ and provides the variations of the critical moment increase $[M_{cr}(N_t)/M_{cr}(0)]$ with the ratio $\beta=N_t/M_y$ (relating the applied tension and maximum bending moment values) for span lengths varying from $L=0.5$ m to $L=15$ m. On the other hand, Fig. 5 concerns HEB300 beams with length $L=10$ m and provides curves the $M_{cr}(N_t)/M_{cr}(0)$ vs. β for all the bending moment diagrams considered in this work. Finally, Fig. 6 concerns $L=15$ m beams with various cross-sections

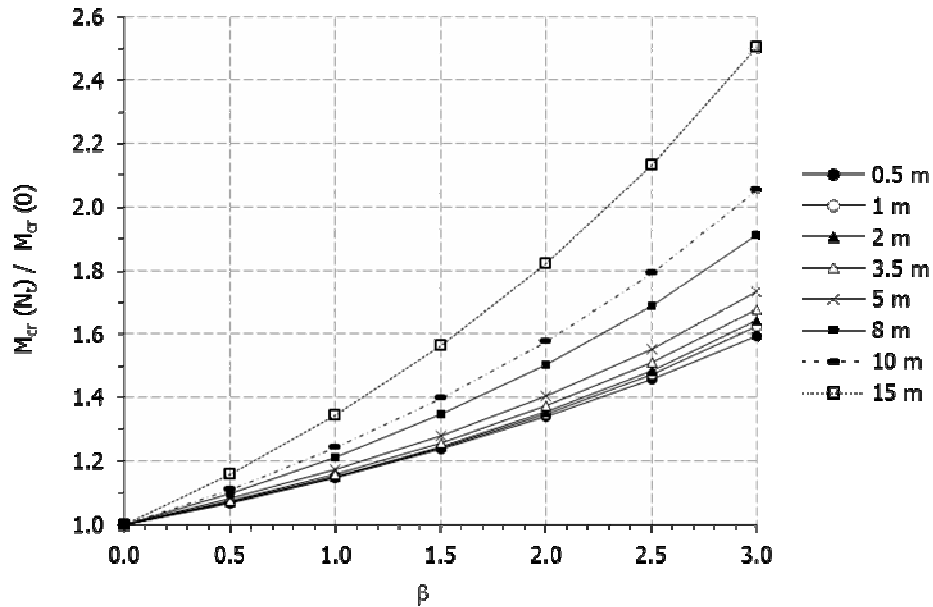


Figure 4: Variation of $M_{cr}(N_t)/M_{cr}(0)$ with β for 0.5 m $\leq L \leq 15$ m (IPE300 beams + $\psi=0$)

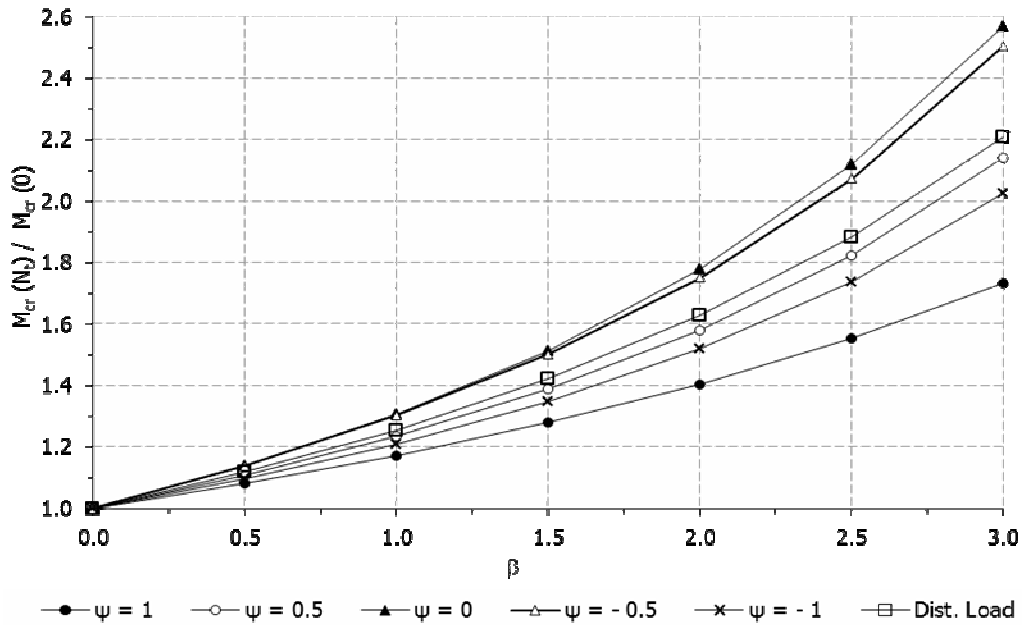


Figure 5: Variation of $M_{cr}(N_t)/M_{cr}(0)$ with β for various moment diagrams (HEB300 beams + $L=10m$)

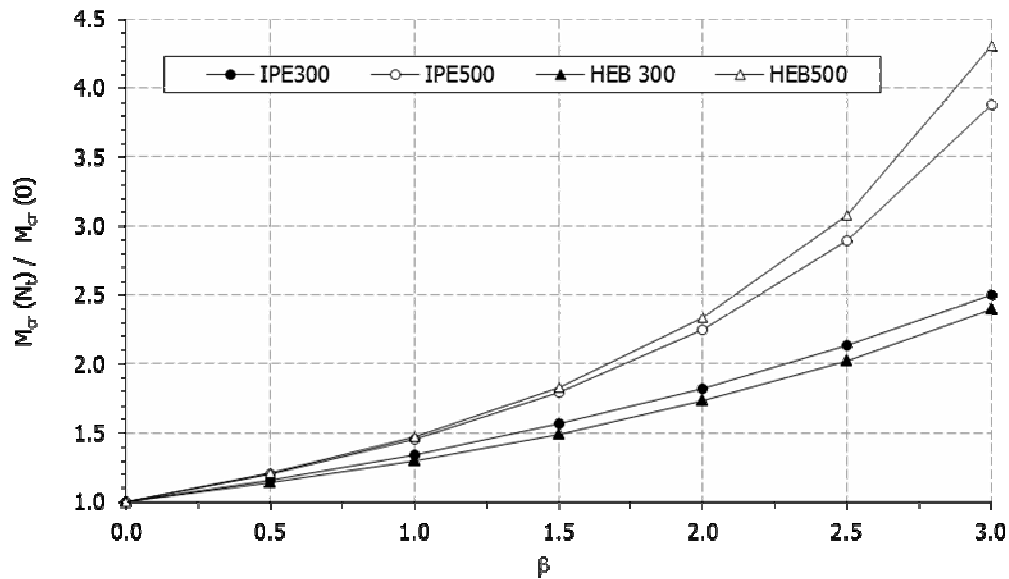


Figure 6: Variation of $M_{cr}(N_t)/M_{cr}(0)$ with β for different cross sections ($L=15m + \psi=0$)

acted by one end moment ($\psi=0$) and shows additional $M_{cr}(N_t)/M_{cr}(0)$ vs. β curves. The observation of the results presented in these three figures, as well as those not shown here but reported by Tomás (2013), prompts the following comments:

- (i) Naturally, the critical moment increase always grows with β , *i.e.*, the amount of tension acting on the beam. Note that, eventually, the $M_{cr}(N_t)/M_{cr}(0)$ vs. β curves would tend to infinity as β approaches the “limit tension value” – the value ensuring that no beam cross-section is acted by compressive stresses. Note, however, that a N_t value established *a priori*, corresponding to the application of transverse loading on a “pre-tensioned” beam, never precludes the occurrence of elastic lateral-torsional buckling (for any N_t).

- (ii) The three sets of $M_{cr}(N_t)/M_{cr}(0)$ vs. β curves, corresponding to the variation of either the beam length (Fig. 4), bending moment diagram (Fig. 5) or cross-section shape (Fig. 6), exhibit qualitatively similar trends, which means that it can be argued that the three above factors are equally relevant.
- (iii) Fig. 4 shows that, logically, the importance of the tension effects grows with the beam length, *i.e.*, as the beam becomes more prone to lateral-torsional instability.
- (iv) Fig. 5 makes it possible to assess how the (beneficial) tension effects vary with the bending moment diagram shape³. The key factor is the shape of the axial force diagram acting on the whole beam compression flange, combining the constant tensile value N_t with varying compressive values due to the bending moments. It is observed that this combination leads to tension effects that are (iv₁) highest for the $\psi=0$ triangular diagram (“least compressed” compression flange) (iv₂) lowest for the $\psi=1$ uniform diagram (“most compressed” compression flange). It is interesting to note that the curve associated with the uniformly distributed load falls, somewhat surprisingly, in between those concerning the $\psi=-0.5$ and $\psi=0.5$ diagrams.
- (v) Finally, Fig. 6 provides clear evidence that the relevance of the tension effects grows considerably with the web height. On the other hand, no conclusion can be drawn about the influence of the flange width, which seems to depend also on the web height.

It is worth noting that the numerical investigation just reported made it possible to gather a critical buckling moment data bank comprising about 1000 values. They will be used later, in section 5, addressing the development of a design procedure for beams subjected to tension.

3. Behaviour and Ultimate Strength – Experimental/Numerical Investigation

This section addresses a limited experimental investigation (only two full-scale tests are reported) on the behavior and ultimate strength of beams subjected to tension. Besides acquiring deeper knowledge about the structural response of these members, this study aims at gathering information intended to develop accurate and reliable numerical (finite element) models. These numerical models will be subsequently employed to carry out parametric studies to assemble a fairly large ultimate strength data bank (see section 4), intended to assess the merits of the design developed in section 5.

After describing the experimental set-up and procedure, including all the measurements, the paper presents and discusses the test results. Finally, the development of the finite element models is addressed – these models are validated by means of the comparison between the test results reported and the corresponding numerical simulations.

3.1 Experimental Set-Up and Procedure

Figs. 7(a)-(b) provide an overall picture of experimental set-up and a detailed view of the beam end support conditions, which combine (i) “fork-type conditions”, with respect to major and minor-axis bending, with (ii) warping restraint of the end cross-sections (the beam “extends” beyond the cross-sections where the end supports are deemed materialized). The two beams tested had length $L=4.00m$ (due to space constraints, the effective beam “free length” was $L=3.36 m$) and were linked at both ends (symmetrically) to rigid secondary systems conceived to ensure a smooth application of eccentric tension (minor-axis eccentricity causing major-axis bending) – see Fig. 8. The tests involved (i) an IPE 200 beam loaded with a $0.25m$ eccentricity, and (ii) a HEA 160 beam loaded with a $0.5m$ eccentricity.

³ Note that the curves provide critical buckling moment percentage increases (not the values).

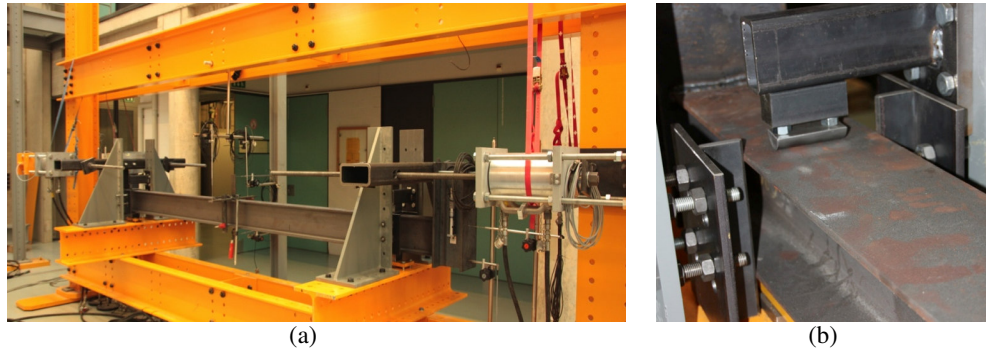


Figure 7: Experimental set-up (a) overall view and (b) detail of the end supports

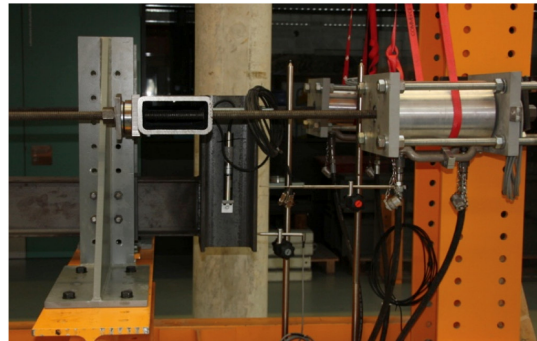


Figure 8: Procedure associated with the application of the eccentric tensile load

Prior to the performance of each test, (i) tensile coupon tests were carried out, in order to assess the real steel material behavior, (ii) the residual stress distribution and magnitude were quantified, by dividing (cutting) the profile into several strips and measuring their individual elongations, and (iii) the specimen initial geometrical imperfections (global and local) were assessed – this was done by measuring, at 10cm intervals along the specimen length, vertical displacements at three upper flange points (web-flange corner and flange free ends) and lateral displacements at three web points (mid-height and web-flange corners).

When performing a test, the first steps consisted of (i) welding vertical rigid profiles to the specimen ends (see Fig. 7(a)), which prevent warping and make it possible to apply the eccentric tensile loads, (ii) positioning the specimen in between two pairs of end support cylindrical hinges, one resting on the supporting cross-bar and the other leaning vertically against a short RHS cantilever (see Fig. 7(b))⁴, making sure that symmetry with respect to the mid cross-section is kept, *i.e.*, that the outstand segments extending beyond each hinge are equal (see Fig. 7(a), and (iii) placing the hydraulic jacks, which are mounted on secondary structural systems, in such a way that the required tension eccentricity is guaranteed (see Fig. 8). The second steps concern the placement of the measuring devices at the mid-span and end cross-sections. In view of the expected specimen three-dimensional behavior, a complex displacement transducer system was devised to enable the measurement of two pairs of mid-span cross-section transverse displacements (two vertical and two lateral) – Fig. 9(a) makes it possible to visualize this displacement transducer system. Moreover, inclinometers were attached to the vertical rigid profiles welded to the specimen ends, in order to measure the major-axis flexural rotations on the supports, as illustrated in Fig. 9(b). During the test, the above measurement devices recorded values at 0.5 second intervals, thus providing a fairly

⁴ This support arrangement ensures free major/minor flexural rotations. Moreover, two pairs of short (rigid) steel plates were placed laterally near each support (see Fig. 7(b)), to limit the end section minor flexural rotations.

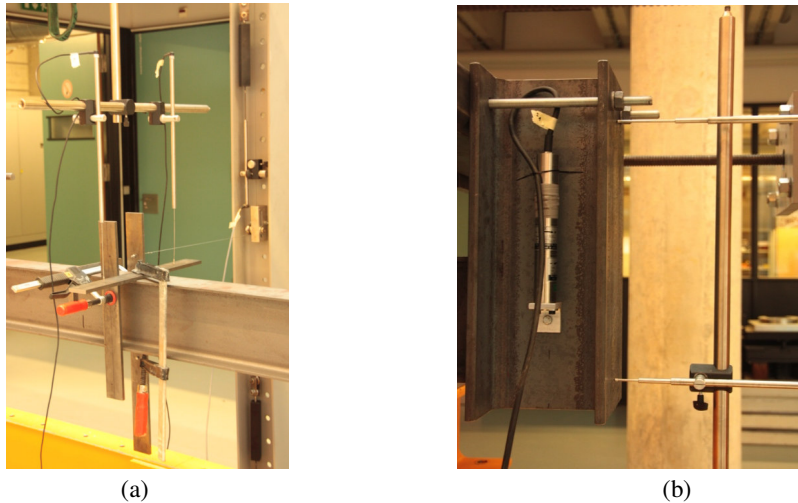


Figure 9: (a) Mid-span displacement sensor system at and (b) inclinometer measuring support flexural rotations

nice continuous displacement/rotation output. Concerning the loading, a two-stage strategy was adopted: (i) large load increments in the elastic range and (ii) much smaller increments after the (expected) onset of yielding, detected by closely monitoring the tensile load level provided by loads cells also at 0.5 second intervals. The specimens were tested up to failure, which means that experimental ultimate loads were obtained.

3.2 Test Results

Each specimen tested was previously characterized, by determining its (i) Young's modulus (E), yield stress (f_y), ultimate stress (f_u) and ultimate extension (ϵ_u), (ii) longitudinal normal residual stress distribution (iii) global and local initial geometrical imperfections. Due to space limitations, only an illustrative sample of this characterization is provided in Figs. 10 and 11(a)-(b). They concern the IPE200 specimen and show (i) the steel constitutive law (stress-strain curve), (ii) the longitudinal normal residual stress distribution and (ii) the initial vertical displacement longitudinal profiles concerning the three top flange points identified earlier, respectively. A detailed account of all this information can be found in Tomás (2013).

The results obtained during the performance of each test consist of (i) experimental evidence concerning the occurrence of lateral-torsional buckling in beams acted by tension (Figs.

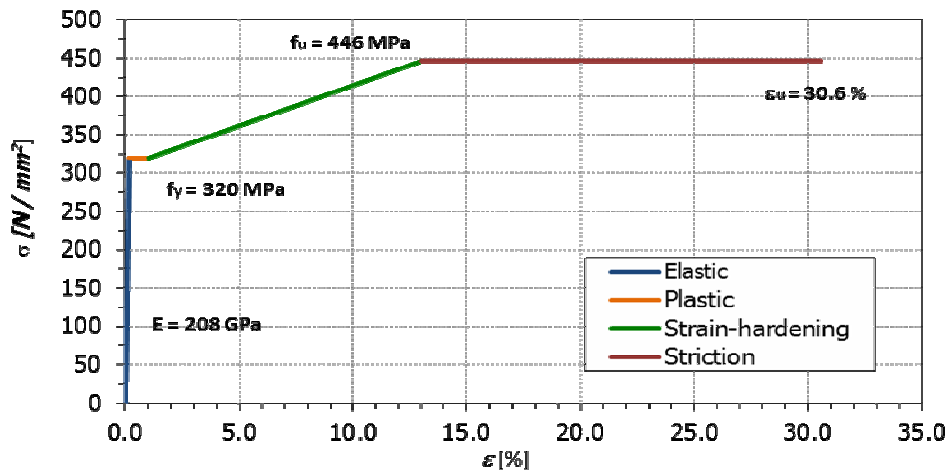


Figure 10: IPE200 specimen steel stress-strain curve (constitutive law)

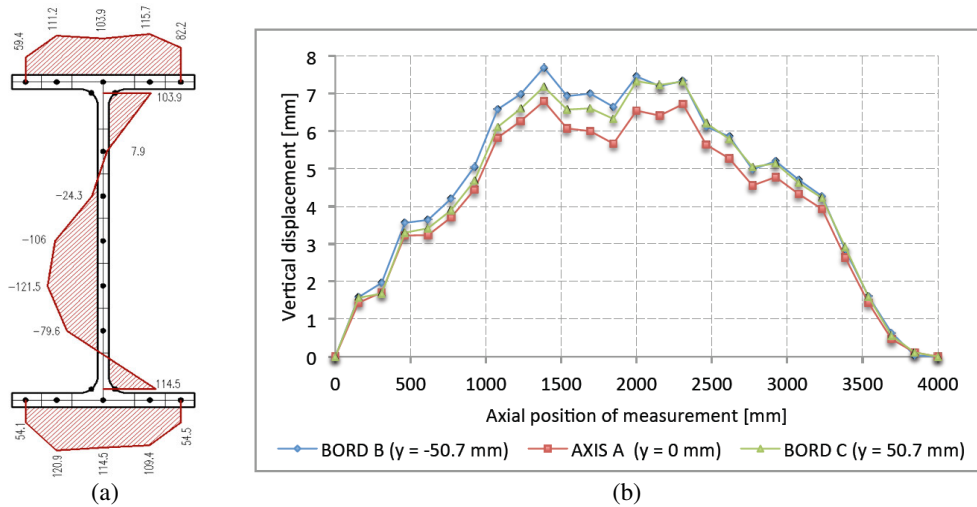


Figure 11: IPE200 specimen (a) longitudinal normal residual stress distribution and (c) initial vertical displacement longitudinal profiles of the three top flange points

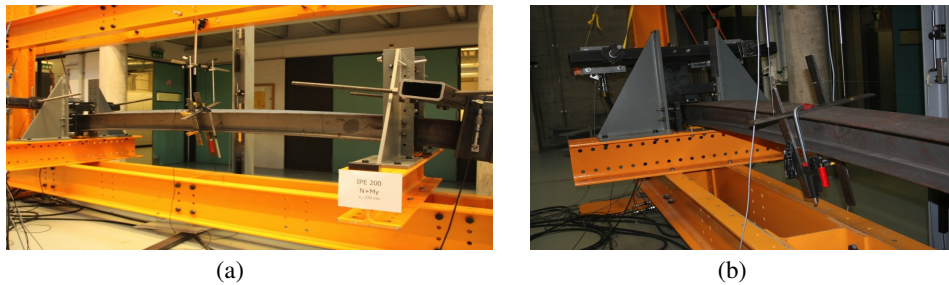


Figure 12: Deformed configurations at the brink of collapse for specimens (a) IPE200 and HEA160

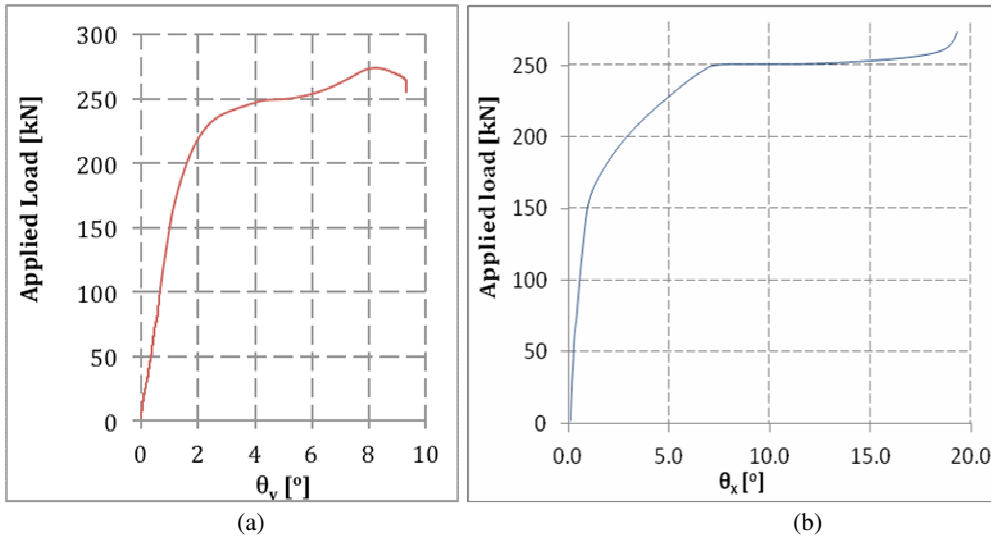


Figure 12: Specimen IPE200 equilibrium paths relating the applied load to (a) the end section flexural rotations θ_v and (b) mid-span torsional rotation θ_x .

The results obtained during the performance of each test consist of (i) experimental evidence concerning the occurrence of lateral-torsional buckling in beams acted by tension (Figs. 12(a)-(b) display the deformed configurations of the IPE200 and HEA160 specimens at the brink of collapse), (ii) equilibrium paths relating the applied load with various measured displacements and/or rotations (Figs. 13(a)-(b) show the IPE200 specimen equilibrium paths

concerning the end cross-section flexural rotation θ_f and mid-span torsional rotation θ_x) and (iii) experimental failure loads: 269.2 kN (IPE200) and 150.0 kN (HEA160).

3.3 Numerical Simulations

The experimental results were also employed to develop, calibrate and validate a shell finite element model able to handle realistic material constitutive laws, end support conditions, load application procedures, initial geometrical imperfections and residual stresses. This was done using the non-linear finite FEM software FINELG (2012), which was originally developed by Ville de Goyet (1989), at the University of Liège, and has been continuously updated by several researchers at that university and also at the Greisch Design Office. In the context of this work, this software was used mainly to perform elastic buckling, elastic-plastic first-order and elastic-plastic second-order analyses. The experimental set-up was entirely modeled with fine meshes of 4-node shell elements based on Kirchhoff's bending theory, thus ensuring that the beam "real end support conditions" and "surroundings" are adequately simulated. Figs. 13 and 14(a)-(b) concern the IPE200 specimen test and provide (i) an overall view of the experimental set-up discretization, (ii) the shape of the initial geometrical imperfections included in the analysis and (iii) the numerical simulation of the load application system.

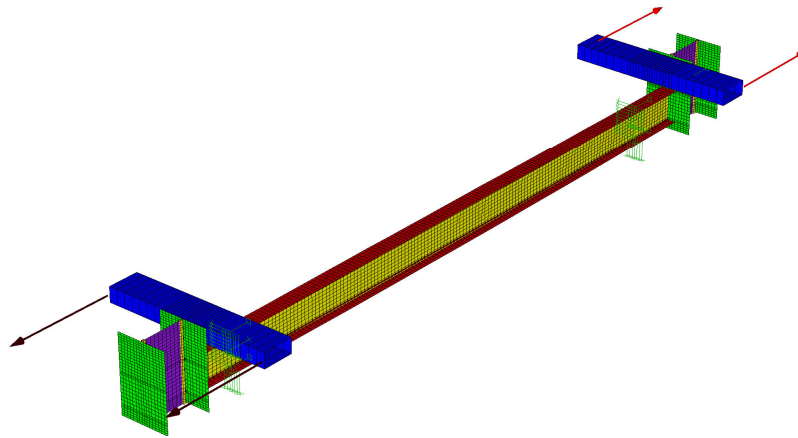


Figure 13: Overall view of the experimental set-up discretization concerning the IPE200 specimen

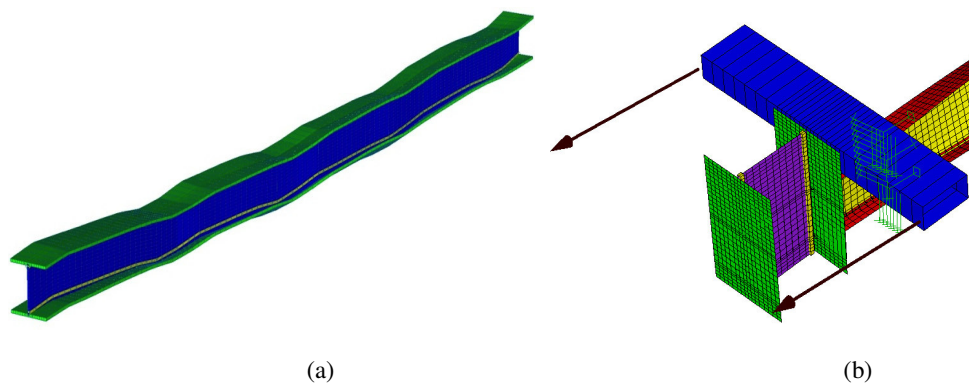


Figure 14: (a) Initial geometrical imperfections (amplified) and (b) load application system models (IPE200)

The developed numerical model was then employed to perform elastic buckling and elastic-plastic geometrically non-linear numerical analyses of the two specimens tested. Table 1 makes it possible to compare the numerical and experimental ultimate moments M_u obtained – moreover, the table also provides the (i) analytical cross-section plastic moments M_{pl} (under pure bending), (ii) FINELG beam critical moments M_{cr} (analyzed in the experimental set-up

context – Fig. 15 displays half of the critical (lateral-torsional) buckling mode shape obtained for the IPE200 specimen) and (iii) beam slenderness values, calculated on the basis of the presented M_{pl} and M_{cr} values – note that both beam are fairly stocky.

Table 1: Analytical, numerical and experimental results concerning the two specimens tested

	M_{pl} [kNm]	$\bar{\lambda}_{LT}[-]$	Numerical		Experimental
			M_{cr} [kNm]	M_u [kNm]	M_u [kNm]
IPE 200	70.6	0.90	86.5	62.98	67.3
HEA 160	75.3	0.66	179	76.9	75

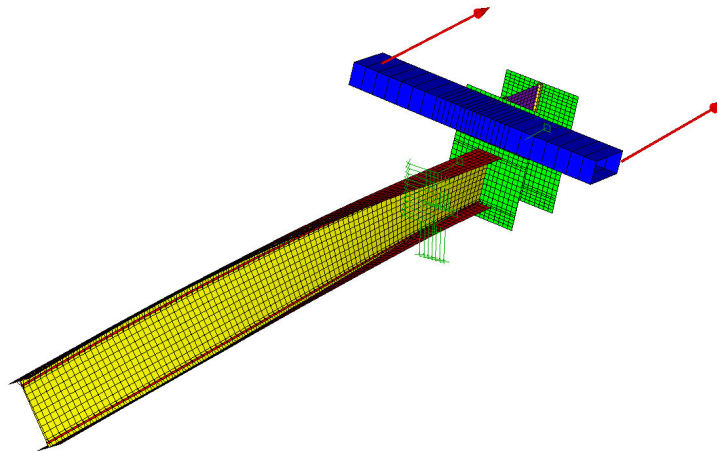


Figure 15: Half of the critical (lateral-torsional) buckling mode provided by FINELG for the IPE200 specimen

The numerical and experimental ultimate moments are found to correlate quite well – indeed, the numerical simulations either underestimate by 6% (IPE200 specimen) or overestimate by 2% (HEA160 specimen) the experimental values. Moreover, Fig. 16 shows the IPE200 specimen deformed configuration at collapse, provided by the FINELG analysis – note the qualitative and quantitative similarity with its experimental counterpart, shown in Fig. 12(a).

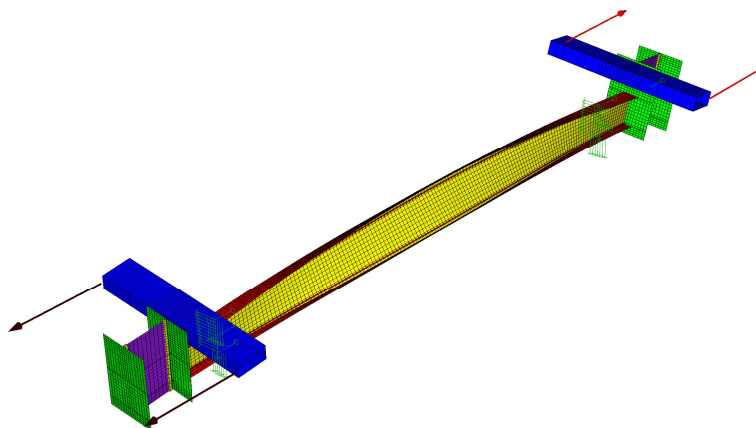


Figure 16: Deformed configuration at collapse obtained with FINELG for the IPE200 specimen

Finally, Figs. 17(a)-(b) compare the experimental equilibrium paths shown in Figs. 12(a)-(b), relating the applied load to the end section flexural rotations and mid-span torsional rotation, with the corresponding numerical simulations. First of all, note that, as mentioned earlier, the numerical and experimental ultimate loads/moments practically coincide (2% difference). Concerning the end section flexural rotations and mid-span torsional rotation, there is a

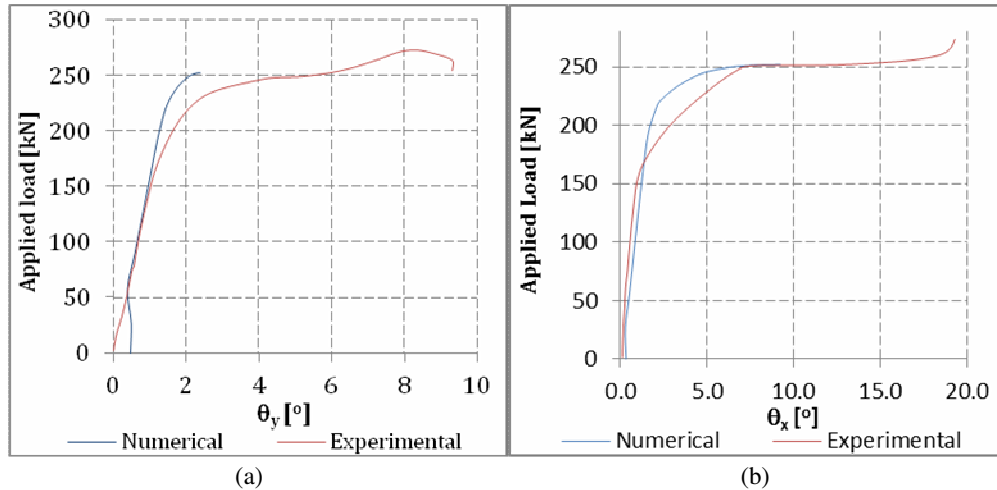


Figure 17: Experimental and numerical equilibrium paths concerning the IPE200 specimen and relating the applied load with the (a) end-section flexural rotations θ_y and (b) mid-span torsional rotation θ_x

virtually perfect coincidence in the elastic regime, beyond which the numerical model is a bit stiffer and, therefore, underestimates the θ_y and θ_x values. A possible explanation for the discrepancies observed between the numerical and experimental equilibrium paths resides in the fact that the three-dimensional nature of the beam deformed configurations may be the source of erroneous measurements. Indeed, it was observed that the accuracy of the transducer measurements decreased considerably when the point under consideration exhibited various displacement components. Although some corrections were made, on the basis of geometry considerations, they gradually become less as the beam deformation increases, rendering almost inevitable the underestimation of the measured displacements and rotations.

On the basis of the comparisons between the test results obtained and the corresponding numerical simulations, most of which were not presented here and can be found in Tomás (2013), it seems fair to conclude that the numerical (shell finite element) model developed provides reasonably accurate results and, thus, can be adequately used to validate the finite element beam model employed to perform the parametric study addressed in the next section.

4. Ultimate Strength Data Bank– Numerical Simulations

The beam and shell finite element models just developed is now employed to perform about 2000 geometrically and materially non-linear analyses of beams under tension containing initial geometrical imperfections and residual stresses (these analyses are often identified by the acronym GMNIA). The parametric studies carried out comprise beams exhibiting several slenderness values, stemming from (i) 8 span lengths (between 0.5 and 25m), (ii) two yield stresses ($f_y=355; 460 MPa$ – the steel material behavior modeled is depicted in Fig. 18 and corresponds to the usual elastic-perfectly plastic constitutively with a marginal strain-hardening occurring for very large strains) and (iii) four cross-section shapes (IPE300, IPE500, HEB300, HEB500). The beams are subjected to (i) five bending moment diagrams ($\psi=1; 0.5, 0, -0.5, -1$) and (ii) six tension levels, corresponding to $\beta=N_t/M_y$ ratios equal to 0; 0.5; 0.75; 1.0; 1.5; 2.0 – a total of over 2000 numerical simulations were carried out. Finally, the beams contain (i) longitudinal normal residual stresses with the parabolic pattern depicted in Fig. 19(a) (values expressed as percentages of $f_y=235 MPa$), and (ii) global sinusoidal initial geometrical imperfections that combine minor-axis flexure and torsion, and exhibit the amplitude (mid-span value) given in Fig. 19(b) – these shapes and values were recently proposed by Boissonnade & Somja (2012). The non-linear analyses were carried out in

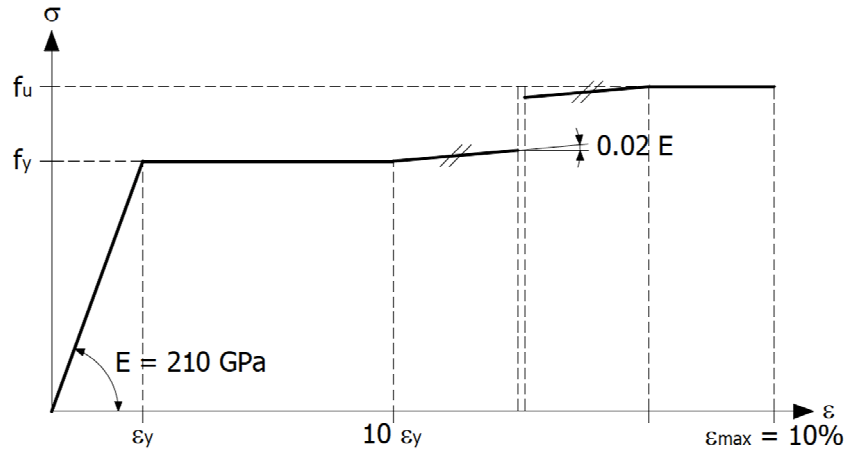


Figure 18: Constitutive law adopted to model the steel material behavior (Boissonnade & Somja 2012)

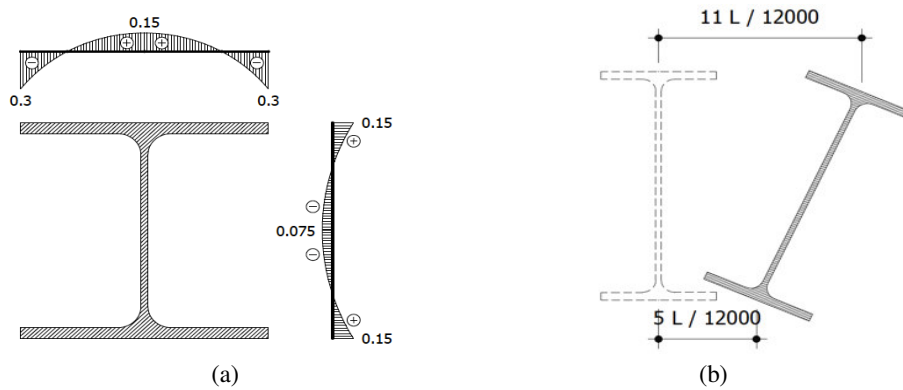


Figure 19: (a) Residual stresses and (b) global initial geometrical imperfections considered in the numerical analyses performed in the context of the parametric study (Boissonnade & Somja 2012)

FINELG and the beams were discretized into standard 3D beam finite elements based on Vlasov's theory for open-section thin-walled members⁵.

Due to space limitations, only a small (but representative) fraction of the results obtained from the above parametric study can be shown in this paper, namely in Figs. 20-22 and Annex A (tabular form – Tables A1-A4) – they concern the results obtained for (i) $L=15m$ S355 IPE300, (ii) $L=5m$ S460 IPE500, (iii) $L=10m$ S355 HEB300 and (iv) $L=3.5m$ S355 HEB500 beams, all subjected to the various bending moment diagrams. Again, a detailed report of the whole set of determined results can be found in Tomás (2013). The results displayed in Figs. 20 and 21 concern the influence of the axial tension level on the ultimate strength of IPE300 and HEB300 beams made of S460 steel, exhibiting various lengths, comprised between $L=0.5m$ and $L=15m$, and subjected to several bending moment diagrams, all stemming from applied end moments. Both figures provide the variation of the ultimate moment M_u , normalized with respect to the cross-section plastic bending resistance M_{pl} (calculated for pure bending on the basis of f_y), with the loading ratio $\beta=N_t/M_y$ – the values between parentheses, given above or below each point (beam analyzed) provide the M_u percentage increase due to axial tension: $[M_u(\beta)-M_u(0)]/M_u(0)$. While Fig. 20 focuses on the combined effect of β and the beam length (under uniform bending), Fig. 21 addresses the

⁵ For validation purposes, the results obtained from FINELG beam and shell finite element analyses were compared – the latter were based on the model validated against the experimental results (see section 3). Provided that the beam length is long enough to preclude local buckling effects, a virtually perfect match was found.

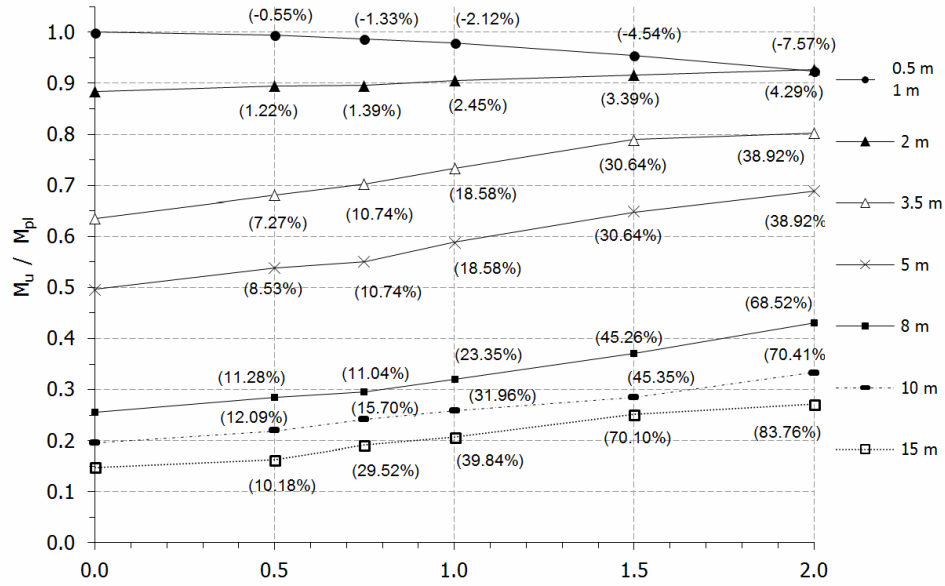


Figure 20: Variation of M_u/M_{pl} with β and the beam length (S460 steel IPE300 beams under uniform bending)

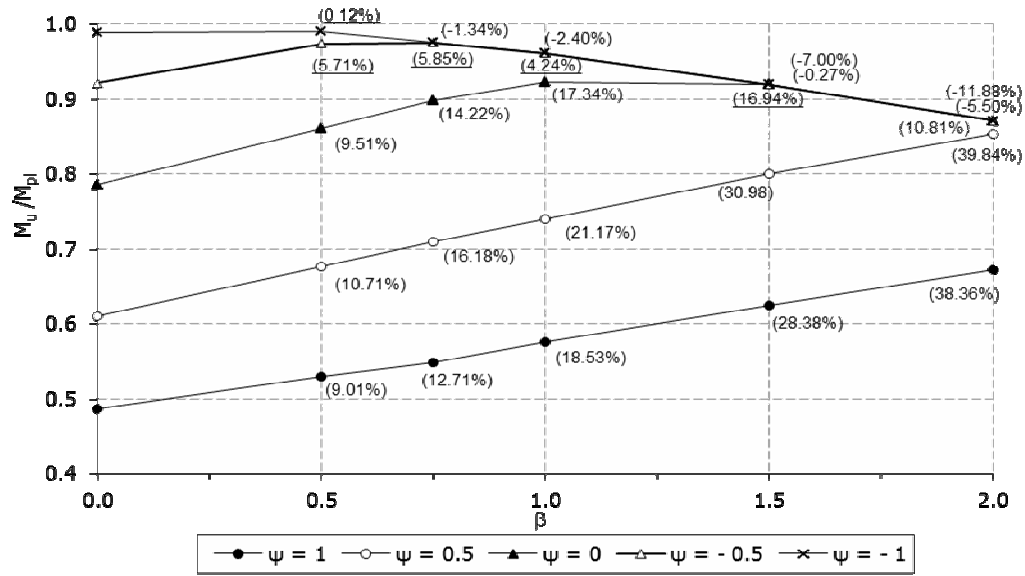


Figure 21: Variation of M_u/M_{pl} with β and the bending moment diagram ($L=15m$ S355 steel HEB300 beams)

joint influence of β and the bending moment diagram (for a $L=15m$ beam). It is worth noting that the negative and underlined positive values in Figs. 20 and 21 correspond to beams whose collapse is governed by the cross-section resistance, which naturally decreases with β^6 . The observation of the numerical results displayed in these figures, as well as those not shown here but reported by Tomás (2013), makes it possible to draw the following conclusions:

- (i) First of all, as expected, the presence of axial tension is completely different in the stocky and slender beams, in the sense that their collapse is governed by plasticity and

⁶ The M_u values provided in Tables A1-A4 are those that effectively correspond to the limit points obtained from the FINELG non-linear analyses, which take into account the small strain-hardening depicted in Fig. 18. However, the M_u values displayed in Fig. 20 are limited by the cross-section resistance determined analytically, which is given in Tables A1-A4 (see the $M_{N,Rk}$ values) and neglects any strain hardening.

instability effects, respectively. In the former (*e.g.*, the $L=0.5; 1.0m$ beams in Fig. 20), axial tension leads to an ultimate moment decrease, stemming exclusively from the drop in cross-section resistance. In the latter (*e.g.*, the $L=8; 10; 15m$ beams in Fig. 20), axial tension leads to an ultimate moment increase, which grows with β and stems from the improved lateral-torsional buckling resistance.

- (ii) The comparison between the M_u/M_{pl} vs. β curves concerning the (ii₁) $L=8; 10; 15m$ and (ii₂) $L=3.5; 5m$ beams show different trends, even if all these curves have positive slopes throughout the whole β range considered. While in the former M_u/M_{pl} grows with β at an always increasing rate (upward curvature), which becomes percentage-wise more relevant as L increases, the latter exhibit points of inflexion, *i.e.*, the curvature changes from upward to downward at a given β value that seems to increase with L . These different trends reflect the contradicting influence of axial tension on the lateral-torsional buckling and cross-section resistances: the latter becomes progressively more relevant as β increases and L decreases. This assertion is fully confirmed by looking at the M_u/M_{pl} vs. β curve concerning the $L=2m$ beam, which exhibits very little growth and ends up merging with their $L=0.5; 1.0m$ beam counterparts for $\beta=2.0$ – it would start descending for larger β values, whenever collapse would start being governed by plasticity in the beam mid-span region.
- (iii) Naturally, the M_u/M_{pl} percentage growth with β is considerably larger for the longer (more slender) beams – *e.g.*, for $L=15m$ and $\beta=2.0$, M_u/M_{pl} increases by almost 85%. (for $L=3.5m$ this same increase is just about 27%).
- (iv) Concerning the influence of the bending moment diagram shape on the axial tension benefit, shown in Fig. 21 for the $L=15m$ S355 steel HEB300 beams, the first important observation is that only the $\psi=1$ and $\psi=0.5$ (marginally) curves (*i.e.*, those leading to more relevant lateral-torsional buckling effects) are not limited by the descending curve associated the mid-span cross-section full yielding up to $\beta=2.0$ – indeed, the $\psi=0$ and $\psi=-0.5$ curves merge into this curve at lower (decreasing) β values and following an “almost horizontal” segment. Finally the $\psi=-1$ curve decreases monotonically with ψ , thus meaning that the beam collapse is always governed by the mid-span cross-section resistance.
- (v) Quantitatively speaking, the highest M_u percentage increases due to the presence of axial tension occur for the beams acted by the $\psi=0.5$ bending moment diagram – they are slightly larger than their $\psi=0$ and $\psi=1$ diagram counterparts (in this order).

Next, Fig. 22 shows how M_u/M_{pl} varies with the beam slenderness $\lambda_{LT}=(M_{pl,Rk}/M_{cr})^{0.5}$, calculated taking into account the axial tension, for various combination of beam length, cross-section shape and steel grade. This figure clearly shows that the net effect of the presence of an increasing axial tension is to move the M_u/M_{pl} vs. λ_{LT} “beam points” (i) to the left (lateral-torsional slenderness decrease) and (ii) upwards (ultimate moment increase), thus reflecting the double influence of N_t . Moreover, it can also be observed in this figure that the whole set of points, corresponding to various beams and β values (including $\beta=0$), remain nicely “aligned” along a “design-like” curve. The design approach for beams subjected to tension that is proposed in the next section takes advantage of this feature. Moreover, this design approach it will be validated against the extensive ultimate moment data bank obtained by means of the parametric study that was just (partially) reported.

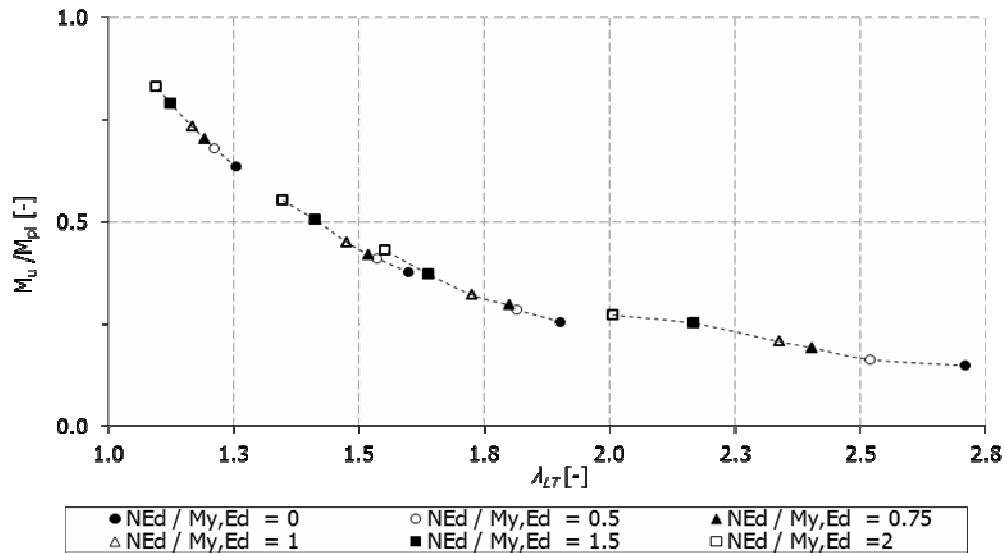


Figure 22: Variation of M_u/M_{pl} with the beam slenderness λ_{LT}

5. Proposed Design Approach

As mentioned earlier, Eurocode 3 (EC3 – CEN 2005) currently lacks design guidance for beams susceptible to lateral-torsional buckling and subjected to tension⁷ – moreover, this topic has also very seldom been addressed in the literature. This means that EC3 completely neglects the beneficial influence of axial tension on the beam ultimate strength, thus leading to overly conservative designs. Indeed, a beam subjected to axial tension is designed against lateral-torsional instability ultimate limit states as “pure beam” (*i.e.*, only major-axis bending is taken into account), and the (detrimental) influence of axial tension is only felt through the cross-section resistance. The aim of the design approach proposed in this work is to change the above situation, by incorporating the axial tension effects in the ultimate moment prediction prescribed by EC3 for compact⁸ hot-rolled steel beams (the so-called “special method”⁹). The proposed design approach is based on the current EC3 methodology, which stipulates that the ultimate moment of (compact) beams subjected to axial tension is the least of two values: (i) the cross-section reduced plastic moment and (ii) the beam bending resistance against a failure stemming from lateral-torsional buckling. While the former is determined through classical strength of materials concepts, the latter is obtained by means of a procedure based on the use of “beam strength curves”. This procedure involves the following steps (the EC3 nomenclature is adopted):

- (i) Determine the beam lateral-torsional slenderness $\lambda_{LT}=(M_{pl,Rk}/M_{cr})^{0.5}$, where $M_{pl,Rk}$ is the cross-section plastic moment (bending resistance) and M_{cr} is the beam critical buckling moment, which obviously depends on the acting major-axis bending moment diagram.
- (ii) On the basis of λ_{LT} , use the appropriate buckling curve (depends on the cross-section geometry and fabrication process – *curve b* for all the profiles considered in this work) to obtain the reduction factor χ_{LT} .

⁷ Although no investigation was carried on this matter, the authors believe that such design guidance is also missing in the vast majority of the current steel structures codes.

⁸ Class 1 or Class 2, according to the EC3 nomenclature.

⁹ Method applicable only to hot-rolled and “equivalent welded” beams – any other beam must be designed by means of the so-called “general method”, which is more conservative.

- (iii) Further modify/increase the reduction factor obtained in the previous step, by means of the relation $\chi_{LT,mod} = \chi_{LT}/f$, where $f \leq 1.0$ is a parameter that depends on the bending moment diagram and beam slenderness λ_{LT} – it supposedly reflects the influence of the spread of plasticity taking place prior to the beam collapse.
- (iv) Evaluate the beam bending resistance against from lateral-torsional buckling failure, which is termed $M_{b,Rd}$ and given by $M_{b,Rd} = \chi_{LT,mod} \times M_{pl,Rk}$.

The proposed design approach consists of merely incorporating the axial tension beneficial effects into the above procedure. This is done exclusively through the value of the critical buckling moment used to determine the beam slenderness, while keeping all the remaining steps unchanged – in particular, $M_{pl,Rk}$ still remains the cross-section pure bending resistance (*i.e.*, does not account for the presence of axial tension). In other words, $M_{cr} \equiv M_{cr}(0)$ is replaced by $M_{cr}(N_{t,Ed})$, where $N_{t,Ed}$ is the acting axial tension, which implies a λ_{LT} decrease and, therefore, also larger $\chi_{LT,mod}$ and $M_{b,Rd}$ values. It is worth noting that the calculation of $M_{cr}(N_{t,Ed})$ must be done by means of a numerical beam buckling analysis (*e.g.*, using beam finite elements) – in the future, the authors plan to develop analytical expressions and/or other design aids that will render the performance of this task easier and more straightforward.

5.1 Assessment of the Proposed Ultimate Moment Estimates

The assessment of the quality of the ultimate moment estimates provided by the proposed modification of the current EC3 design rules is based on the results of the numerical simulations partially reported in section 4 and shown in Tables A1-A4 – the full set of results can be found in Tomás (2013). These results consist of, for each combination of beam geometry (cross-section and length), steel grade, bending moment diagram and β value, the beam (i) critical moment M_{cr} (accounting for the axial tension) (ii) plastic moment $M_{pl,Rk}$, (iii) reduced (by the axial tension) plastic bending resistance $M_{N,Rk}$, (iv) numerical ultimate moment M_u (v) lateral-torsional slenderness λ_{LT} (based on M_{cr} and $M_{pl,Rk}$), (vi) reduction factor $\chi_{LT,mod}$ (obtained with the EC3 *curve b*), (vii) predicted ultimate moment $M_{b,Rd}$ (for a lateral-torsional failure) and (viii) numerical-to-estimated moment ratio $R_M = M_u / M_{u,est}$, where $M_{u,est}$ is the lower between $M_{N,Rk}$ and $M_{b,Rd}$ – whenever $M_{u,est} = M_{N,Rk}$, the value of R_M reflects the cross-section over-strength due to the small strain-hardening included in the steel constitutive law modeled in this work.

Before comparing the obtained numerical and estimated ultimate moments, it should be pointed out that this comparison concerns exclusively the beams whose collapse does not correspond to exhausting the beam mid-span cross-section resistance, *i.e.*, beams failing in lateral-torsional modes occurring prior to the attainment of $M_{N,Rk}$ – indeed, the proposed design approach only concern the latter. Figs. 23 to 25 concern the various columns analyzed under bending moment diagrams defined by $\psi = 1$, $\psi = 0$ and $\psi = -1$, respectively, and make it possible to compare the numerical ultimate moments with their predictions provided by the proposed design approach – use of the EC3 design *curve b* with a lateral-torsional slenderness modified through the inclusion of the critical buckling dependence on N_t . The observation of these three figures prompts the following remarks:

- (i) First of all, it is worth noting that the length of the EC3 design *curve b* horizontal plateau depends on the bending moment diagram acting on the beam – indeed, this plateau length increases from 0.4 ($\psi = 1$) to 0.70 ($\psi = 0$) and 0.80 ($\psi = -1$).
- (ii) Then, it is impossible not to notice the remarkable closeness between the numerical ultimate moments and their predictions provided by the proposed design approach. Indeed, in the three figures the numerical values are virtually aligned on top the design

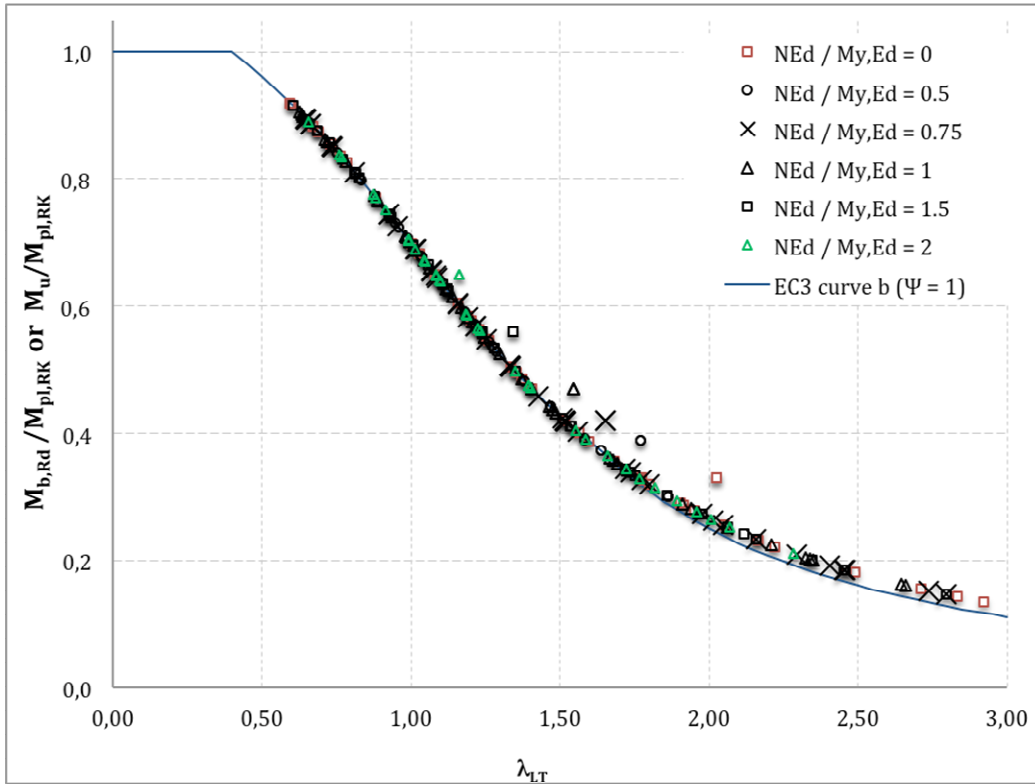


Figure 23: Comparison between the $M_u/M_{pl,Rk}$ (numerical) and $M_{b,Rd}/M_{pl,Rk}$ (proposed design approach) for $\psi=1$

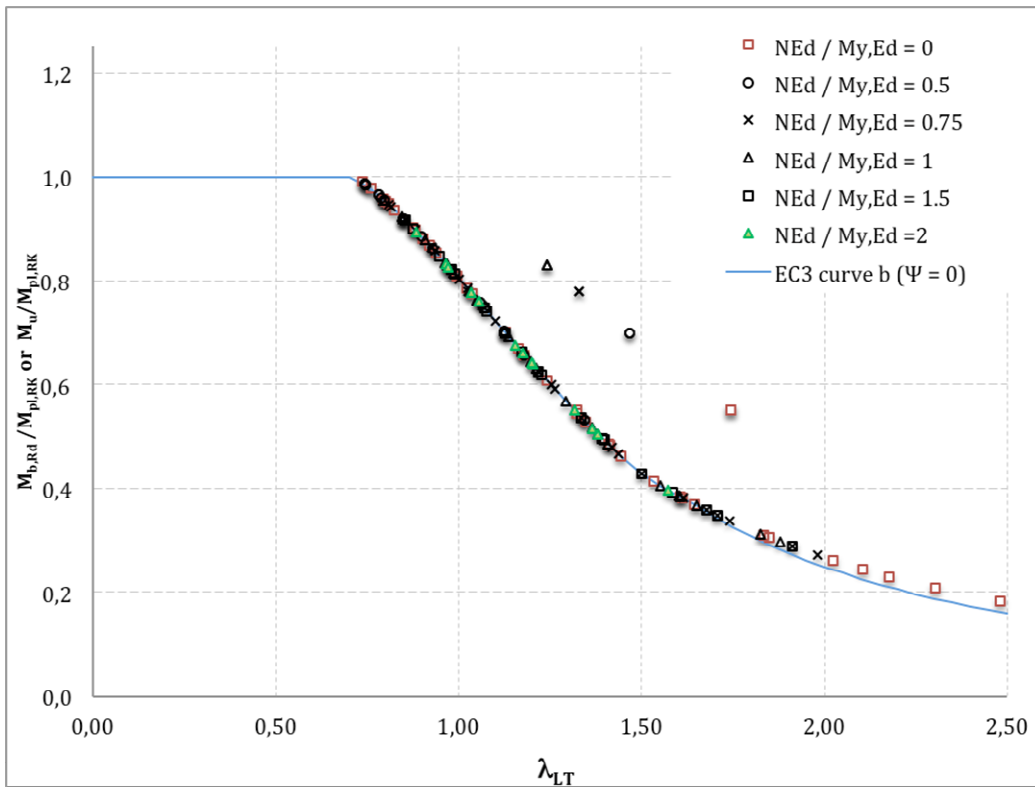


Figure 34: Comparison between the $M_u/M_{pl,Rk}$ (numerical) and $M_{b,Rd}/M_{pl,Rk}$ (proposed design approach) for $\psi=0$

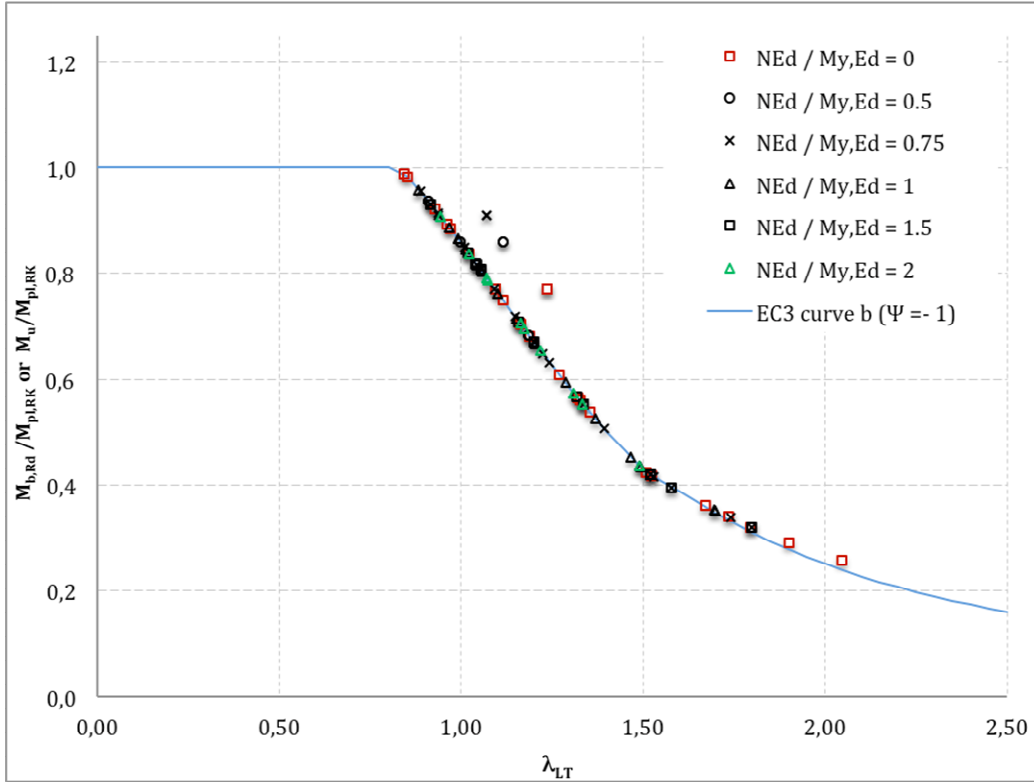


Figure 25: Comparison between the $M_u/M_{pl,Rk}$ (numerical) and $M_{b,Rd}/M_{pl,Rk}$ (proposed design approach) for $\psi=-1$

curve – it is only possible to detect a very slight underestimation in the high slenderness range (it grows with λ_{LT}), particularly for $\psi=1$ (heavier lateral-torsional buckling effects).

- (iii) However, it is equally impossible not to notice the few striking exceptions to the very general rule put forward in the previous item. They all concern the same beam: an $L=25m$ S460 steel HEB500 beam. The explanation for these discrepancies lies in the fact that, for most loadings (*i.e.*, whenever the mid-span cross-section resistance does not govern), this beam collapses at extremely high deformation levels (*e.g.*, torsional rotations above 90°), associated to ultimate moments that are clearly underestimated by the design curve, particularly for $\psi=0$. If the ultimate moments were linked to “acceptable deformation levels” (instead of actual equilibrium path limit points) their values would drop and end up much closer to the design curve. For instance, if the (perfectly logical) torsional rotation limit of 15° was adopted as a beam ultimate limit state, all the $M_u/M_{pl,Rk}$ values associated with the beam under consideration would be no more than about 12% above the EC3 design curve *b* (value for $\psi=0$ and $\beta=1$).
- (iv) Table 2 provides the averages, standard deviations and maximum/minimum values of the ratio $R_M=M_u/M_{u,est}$ corresponding to Figs. 23-25 and for the various axial tension

Table 2: Averages, standard deviations and maximum/minimum value of the ratio R_M

	Average	St. Dev.	Max	Min
$\beta=0$	1.08	0.06	1.17	0.98
$\beta=0.5$	1.04	0.09	1.11	0.97
$\beta=0.75$	1.07	0.10	1.16	0.94
$\beta=1$	1.05	0.12	1.09	0.95
$\beta=1.5$	1.02	0.08	1.08	0.96
$\beta=2$	1.02	0.04	1.08	0.93

levels (excluding the 13 $L=25m$ S460 steel HEB500 beam ultimate moments). These indicators reflect the excellent quality of the ultimate moment estimates – indeed, the overwhelming majority of them are safe and extremely accurate. It is still worth noticing that the least accurate estimations (higher average and standard deviation) concern $\beta=1$.

In view of what was mentioned above, it seems fair to conclude that the proposed design approach for beams subjected to torsion provides excellent estimates of all the numerical ultimate moments obtained in this work (associated with lateral-torsional collapse modes) and, therefore, can be considered as a very promising candidate for inclusion in a future version of Eurocode 3 – of course, additional parametric and reliability studies are needed before this goal can be achieved. The only foreseeable hurdle for designers is the lack of an easy and user-friendly way to calculate critical buckling moment in the presence of axial tension – as mentioned earlier, the authors plan to work on the removal of this hurdle through the development of analytical expressions and/or other design aids to calculate $M_{cr}(N_t, E_d)$.

5.2 Axial Tension Beneficial Influence

In order to assess the beneficial influence of the presence of axial tension on the beam ultimate strength/moment, let us begin by considering a $L=8.0m$ S355 steel IPE500 beam subjected to uniform bending and six axial tension levels (β values). Table 3 shows the corresponding λ_{LT} , $\chi_{LT,mod}$ and $M_{b,Rd}$ values, and also the $M_{b,Rd}$ percentage increases with respect to the “pure bending” value ($\Delta M_{b,Rd}$). Fig. 26 provides a pictorial representation of the various $M_{b,Rd}$ and $\Delta M_{b,Rd}$ values – it is very clear that how an increase in axial loading causes a slenderness drop and the corresponding ultimate moment increase. In order to assess the beneficial influence of the presence of axial tension on the beam ultimate

Finally, Table 4 provides the averages, standard deviations and maximum/minimum values of the percentage ultimate moment increases ($\Delta M_{b,Rd}$) due to axial tension corresponding to Figs. 23-25 and excluding again the 13 $L=25m$ S460 steel HEB500 beam ultimate moments. It is observed that all the above axial tension benefit indicators increase with β , with the sole exception of the minimum value – it remains constant and very small, because it always corresponds to a slenderness located very close to the end of the design curve plateau.

Table 3: Ultimate moment predictions for the $L=8.0m$ S355 steel IPE500 beam under uniform bending

β	λ_{LT}	$\chi_{LT,mod}$	$M_{b,Rd}$ [kNm]	$\Delta M_{b,Rd}$ [kNm]
0	1.683	0.357	278.1	–
0.5	1.575	0.396	308.9	30.8%
0.75	1.509	0.423	329.9	51.8%
1	1.464	0.443	345.1	67%
1.5	1.350	0.498	387.8	109.7%
2	1.231	0.562	437.8	159.7%

Table 4: Averages, standard deviations and maximum/minimum values of $\Delta M_{b,Rd}$

β	Average	St. Dev.	Max	Min
$\beta=0.5$	12.6%	7.6%	33%	0.94%
$\beta=0.75$	17.3%	10.7%	45%	0.94%
$\beta=1$	25.2%	16.7%	71%	0.94%
$\beta=1.5$	38.8%	28.3%	117%	0.94%
$\beta=2$	52.8%	42.5%	183%	0.94%

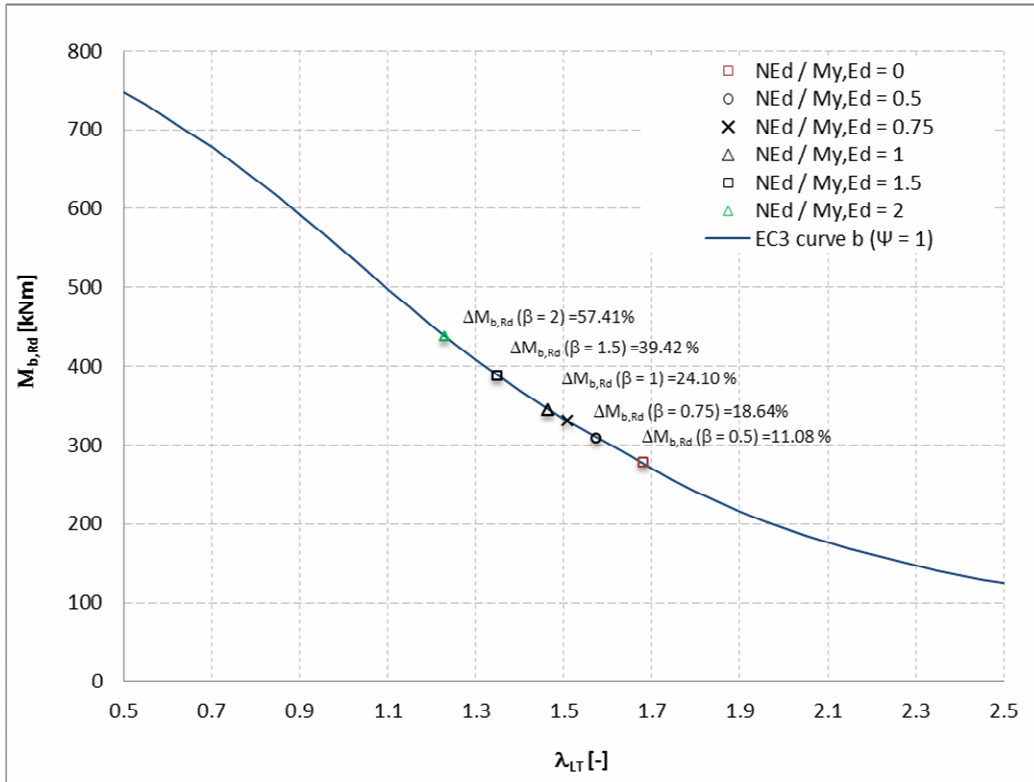


Figure 26: Pictorial representation of the ultimate moment predictions – $L=8.0m$ S355 steel IPE500 beam ($\psi=1$)

Conclusion

This paper reported the results of an analytical, numerical and experimental investigation on the lateral-torsional stability, failure and design of hot-rolled steel I-section beams with fork-type end supports and acted by simple transverse loadings (mostly applied end moments) and various axial tension values. Initially, the derivation and validation of an analytical expression providing critical buckling moments of uniformly bent beams subjected to tension was presented. Then, this analytical finding was followed by a numerical study on the beneficial influence of axial tension on beams under non-uniform bending, namely caused by unequal applied end moments or a uniformly distributed load – several beam finite element results were presented and discussed in some detail. Next, the paper addressed the performance of two experimental tests, carried out at the University of Fribourg and aimed at determining the behavior and ultimate strength of a narrow and a wide flange beams subjected to eccentric axial tension. The experimental set-up and procedure were described, and the main results obtained (initial imperfection and residual stress measurements, and beam equilibrium paths) were displayed and briefly commented. These results were also used to develop and validate FINELG beam and shell finite element models that were subsequently employed to perform an extensive parametric study that (i) involved more than 2000 numerical simulations, concerning beams with various cross-section shapes, lengths, yield stresses, acting bending moment diagrams and axial tension levels, and (ii) was carried to gather a fairly large ultimate strength/moment data bank. Finally, these data were then used to assess the merits of a design approach proposed for beams subjected to tension and collapsing in lateral-torsional modes – this design approach consists of slightly modifying the current procedure prescribed in Eurocode 3 to design beams against lateral-torsional failures (through the incorporation of the axial tension influence on the critical buckling moment that is used to evaluate the beam slenderness). The ultimate moment estimates provided by proposed design approach were

shown to correlate extremely well with the values obtained from the numerical simulations, thus making it a very promising candidate for inclusion in a future version of Eurocode 3. Lastly, the paper closed with a quick assessment of the beneficial influence of axial tension on the ultimate strength/moment of beams failing in lateral-torsional modes – as expected, it was found that this influence can be quite significant and, thus, neglecting it (as is currently done in practically all steel structures codes) will certainly lead to over-conservative designs.

References

- Boissonnade N. Greiner R. Jaspart JP. Lindner J (2006). *Rules for Member Stability in EN 1993-1-1: Background Documentation and Design Guidelines* (ECSS Technical Committee 8 – Stability). ECCS Publication N° 119.
- Boissonnade N. Somja H (2012). “Influence of imperfections in FEM modeling of lateral-torsional buckling”. *USB Key Drive Proceedings of SSRC Annual Stability Conference*. (Grapevine. 17-21/4).
- CEN (Comité Européen de Normalisation) (1992). *Eurocode 3: Design of Steel Structures – Part 1.1: General Rules and Rules for Buildings* (ENV 1993-1-1). Brussels.
- CEN (Comité Européen de Normalisation) (2005). *Eurocode 3: Design of Steel Structures – Part 1.1: General Rules and Rules for Buildings* (EN 1993-1-1). Brussels.
- Chen W-F. Atsuta T (1977). *Theory of Beam-Columns – Space Behavior and Design* (vol. 2). McGraw-Hill. New York.
- Culver C (1966). “Exact solution of the biaxial bending equations”. *Journal of the Structural Division* (ASCE). **92**(2), 63-83.
- FINELG (Non-Linear Finite Element Analysis Program) (2012). *User's Manual* (vrs. 9.3). ArGEnCo Department. University of Liège. and Greisch Info S.A.. Liège.
- Simulia Inc. (2008). *Abaqus Standard* (vrs. 6.7-5).
- Tomás J (2013). *I-Section Steel Beams under Tension: Lateral-Torsional Buckling. Ultimate Strength and Design*. M.A.Sc. Thesis in Civil Engineering (Structures). Instituto Superior Técnico. Technical University of Lisbon.
- Trahair NS (1993). *Flexural Torsional Buckling of Structures*. E&FN Spon (Chapman & Hall). London.
- Ville de Goyet V (1989). *L'Analyse Statique Non Linéaire par la Méthode des Éléments Finis des Structures Spatiales Formées de Poutres à Section Symétrique*. Ph.D. Thesis in Applied Science. University of Liège. (French)

ANNEX A

Table A1: Numerical and design results concerning the $L=15m$ S355 steel IPE300 beams

$\psi = 1$

β [m^{-1}]	M_{cr} [kNm]	$M_{pl,Rk}$ [kNm]	$M_{N,Rk}$ [kNm]	M_u [kNm]	λ_{LT}	$\chi_{LT,mod}$	$M_{b,Rd}$ [kNm]	R_M
0	30.405	223.2	223.181	32.968	2.709	0.155	34.7	0.95
0.5	35.186	223.2	221.960	36.325	2.519	0.178	39.6	0.92
0.75	38.636	223.2	220.204	42.700	2.403	0.193	43.1	0.99
1	40.843	223.2	218.448	46.104	2.338	0.203	45.3	1.02
1.5	47.522	223.2	213.051	56.078	2.167	0.232	51.8	1.08
2	55.415	223.2	206.296	60.584	2.007	0.266	59.3	1.02

$\psi = 0.5$

β [m^{-1}]	M_{cr} [kNm]	$M_{pl,Rk}$ [kNm]	$M_{N,Rk}$ [kNm]	M_u [kNm]	λ_{LT}	$\chi_{LT,mod}$	$M_{b,Rd}$ [kNm]	R_M
0	39.960	223.2	223.181	44.456	2.363	0.199	44.4	1.00
0.5	48.157	223.2	221.960	51.639	2.153	0.235	52.5	0.98
0.75	53.904	223.2	220.204	56.490	2.035	0.259	57.9	0.98
1	58.076	223.2	218.448	61.703	1.960	0.277	61.7	1.00
1.5	69.939	223.2	213.051	72.956	1.786	0.324	72.2	1.01
2	84.086	223.2	206.296	89.21	1.629	0.376	83.9	1.06

$\psi = 0$

β [m^{-1}]	M_{cr} [kNm]	$M_{pl,Rk}$ [kNm]	$M_{N,Rk}$ [kNm]	M_u [kNm]	λ_{LT}	$\chi_{LT,mod}$	$M_{b,Rd}$ [kNm]	R_M
0	54.493	223.2	223.181	49.911	2.024	0.262	58.4	0.85
0.5	67.394	223.2	221.960	62.863	1.820	0.314	70.0	0.90
0.75	73.550	223.2	220.204	74.669	1.742	0.337	75.3	0.99
1	81.871	223.2	218.448	82.793	1.651	0.368	82.1	1.01
1.5	98.148	223.2	213.051	124.357	1.508	0.424	94.6	1.31
2	116.957	223.2	206.296	151.009	1.381	0.505	112.7	1.34

$\psi = -0.5$

β [m^{-1}]	M_{cr} [kNm]	$M_{pl,Rk}$ [kNm]	$M_{N,Rk}$ [kNm]	M_u [kNm]	λ_{LT}	$\chi_{LT,mod}$	$M_{b,Rd}$ [kNm]	R_M
0	73.169	223.2	223.181	68.029	1.746	0.336	75.0	0.91
0.5	88.004	223.2	221.960	85.189	1.592	0.390	87.0	0.98
0.75	93.846	223.2	220.204	99.200	1.542	0.410	91.4	1.09
1	103.558	223.2	218.448	114.230	1.468	0.449	100.3	1.14
1.5	121.178	223.2	213.051	132.896	1.357	0.527	117.6	1.13
2	142.143	223.2	206.296	156.140	1.253	0.609	135.8	1.15

$\psi = -1$

β [m^{-1}]	M_{cr} [kNm]	$M_{pl,Rk}$ [kNm]	$M_{N,Rk}$ [kNm]	M_u [kNm]	λ_{LT}	$\chi_{LT,mod}$	$M_{b,Rd}$ [kNm]	R_M
0	80.019	223.2	223.181	83.864	1.670	0.361	80.6	1.04
0.5	89.342	223.2	221.960	87.300	1.581	0.394	88.0	0.99
0.75	95.376	223.2	220.204	97.100	1.530	0.415	92.6	1.05
1	100.443	223.2	218.448	97.604	1.491	0.435	97.1	1.00
1.5	113.825	223.2	213.051	112.552	1.400	0.500	111.7	1.01
2	130.202	223.2	206.296	132.897	1.309	0.574	128.0	1.04

Table A2: Numerical and design results concerning the $L=5m$ S460 steel IPE500 beams

$\psi = 1$

$\beta [m^{-1}]$	$M_{cr} [kNm]$	$M_{pl,Rk} [kNm]$	$M_{N,Rk} [kNm]$	$M_u [kNm]$	λ_{LT}	$\chi_{LT,mod}$	$M_{b,Rd} [kNm]$	R_M
0	552.7	1009.7	1009.7	464.0	1.352	0.497	501.6	0.93
0.5	622.3	1009.7	996.5	524.3	1.274	0.538	542.9	0.97
0.75	681.7	1009.7	978.5	560.5	1.217	0.569	575.0	0.97
1	710.0	1009.7	960.5	602.1	1.192	0.584	589.2	1.02
1.5	824.3	1009.7	910.3	706.5	1.107	0.634	640.6	1.10
2	979.0	1009.7	854.2	790.0	1.016	0.690	696.8	1.13

$\psi = 0.5$

$\beta [m^{-1}]$	$M_{cr} [kNm]$	$M_{pl,Rk} [kNm]$	$M_{N,Rk} [kNm]$	$M_u [kNm]$	λ_{LT}	$\chi_{LT,mod}$	$M_{b,Rd} [kNm]$	R_M
0	729.6	1009.7	1009.7	607.0	1.176	0.625	630.7	0.96
0.5	853.5	1009.7	996.5	710.6	1.088	0.687	693.3	1.02
0.75	978.3	1009.7	978.5	775.8	1.016	0.737	744.4	1.04
1	1022.2	1009.7	960.5	247.3	0.994	0.753	760.0	0.33
1.5	1264.6	1009.7	910.3	268.8	0.894	0.821	828.9	0.32
2	1638.9	1009.7	854.2	279.2	0.785	0.888	896.9	0.31

$\psi = 0$

$\beta [m^{-1}]$	$M_{cr} [kNm]$	$M_{pl,Rk} [kNm]$	$M_{N,Rk} [kNm]$	$M_u [kNm]$	λ_{LT}	$\chi_{LT,mod}$	$M_{b,Rd} [kNm]$	R_M
0	1019.4	1009.7	1009.7	664.7	0.995	0.809	816.9	0.81
0.5	1249.5	1009.7	996.5	721.5	0.899	0.884	892.6	0.81
0.75	1383.4	1009.7	978.5	748.8	0.854	0.916	925.2	0.81
1	1580.9	1009.7	960.5	793.6	0.799	0.953	962.6	0.82
1.5	2084.3	1009.7	910.3	836.6	0.696	0.902	910.3	0.92
2	2901.6	1009.7	854.2	871.0	0.590	0.846	854.2	1.02

$\psi = -0.5$

$\beta [m^{-1}]$	$M_{cr} [kNm]$	$M_{pl,Rk} [kNm]$	$M_{N,Rk} [kNm]$	$M_u [kNm]$	λ_{LT}	$\chi_{LT,mod}$	$M_{b,Rd} [kNm]$	R_M
0	1425.7	1009.7	1009.7	677.9	0.842	0.951	960.0	0.71
0.5	1761.0	1009.7	996.5	723.8	0.757	0.987	996.5	0.73
0.75	2568.5	1009.7	978.5	751.0	0.627	0.969	978.5	0.77
1	2227.2	1009.7	960.5	783.7	0.673	0.951	960.5	0.82
1.5	2920.6	1009.7	910.3	828.3	0.588	0.902	910.3	0.91
2	4044.4	1009.7	854.2	860.6	0.500	0.846	854.2	1.01

$\psi = -1$

$\beta [m^{-1}]$	$M_{cr} [kNm]$	$M_{pl,Rk} [kNm]$	$M_{N,Rk} [kNm]$	$M_u [kNm]$	λ_{LT}	$\chi_{LT,mod}$	$M_{b,Rd} [kNm]$	R_M
0	1505.0	1009.7	1009.7	826.6	0.819	1.000	1009.7	0.82
0.5	1757.9	1009.7	996.5	834.1	0.758	0.987	996.5	0.84
0.75	1806.7	1009.7	978.5	870.4	0.748	0.969	978.5	0.89
1	2104.6	1009.7	960.5	921.1	0.693	0.951	960.5	0.96
1.5	2605.7	1009.7	910.3	951.1	0.622	0.902	910.3	1.04
2	3383.9	1009.7	854.2	972.3	0.546	0.846	854.2	1.14

Table A3: Numerical and design results concerning the $L=10m$ S355 steel HEB300 beams

$\psi = 1$

$\beta [m^{-1}]$	$M_{cr} [kNm]$	$M_{pl,Rk} [kNm]$	$M_{N,Rk} [kNm]$	$M_u [kNm]$	λ_{LT}	$\chi_{LT,mod}$	$M_{b,Rd} [kNm]$	R_M
0	560.1	664.0	664.049	443.2	1.089	0.645	428.5	1.03
0.5	618.8	664.0	657.138	507.5	1.036	0.678	450.0	1.13
0.75	641.7	664.0	647.564	522.2	1.017	0.689	457.6	1.14
1	688.1	664.0	637.991	585.1	0.982	0.710	471.8	1.24
1.5	771.0	664.0	610.382	644.4	0.928	0.743	493.6	1.31
2	871.8	664.0	578.383	798.0	0.873	0.776	515.3	1.55

$\psi = 0.5$

$\beta [m^{-1}]$	$M_{cr} [kNm]$	$M_{pl,Rk} [kNm]$	$M_{N,Rk} [kNm]$	$M_u [kNm]$	λ_{LT}	$\chi_{LT,mod}$	$M_{b,Rd} [kNm]$	R_M
0	737.6	664.0	664.049	565.3	0.949	0.784	520.5	1.09
0.5	839.9	664.0	657.138	644.0	0.889	0.824	547.0	1.18
0.75	899.6	664.0	647.564	665.7	0.859	0.843	559.9	1.19
1	966.3	664.0	637.991	679.5	0.829	0.862	572.4	1.19
1.5	1125.3	664.0	610.382	748.8	0.768	0.898	596.2	1.26
2	1330.4	664.0	578.383	810.4	0.706	0.931	618.3	1.31

$\psi = 0$

$\beta [m^{-1}]$	$M_{cr} [kNm]$	$M_{pl,Rk} [kNm]$	$M_{N,Rk} [kNm]$	$M_u [kNm]$	λ_{LT}	$\chi_{LT,mod}$	$M_{b,Rd} [kNm]$	R_M
0	1016.5	664.0	664.049	665.1	0.808	0.948	629.2	1.06
0.5	1192.2	664.0	657.138	686.7	0.746	0.985	654.4	1.05
0.75	1314.9	664.0	647.564	706.6	0.711	0.975	647.6	1.09
1	1409.8	664.0	637.991	711.6	0.686	0.961	638.0	1.12
1.5	1683.6	664.0	610.382	767.0	0.628	0.919	610.4	1.26
2	2036.3	664.0	578.383	825.1	0.571	0.871	578.4	1.43

$\psi = -0.5$

$\beta [m^{-1}]$	$M_{cr} [kNm]$	$M_{pl,Rk} [kNm]$	$M_{N,Rk} [kNm]$	$M_u [kNm]$	λ_{LT}	$\chi_{LT,mod}$	$M_{b,Rd} [kNm]$	R_M
0	1388.9	664.0	664.049	689.1	0.691	1.000	664.0	1.04
0.5	1619.9	664.0	657.138	703.0	0.640	0.990	657.1	1.07
0.75	1775.0	664.0	647.564	727.0	0.612	0.975	647.6	1.12
1	1893.5	664.0	637.991	737.5	0.592	0.961	638.0	1.16
1.5	2232.3	664.0	610.382	777.6	0.545	0.919	610.4	1.27
2	2671.0	664.0	578.383	825.3	0.499	0.871	578.4	1.43

$\psi = -1$

$\beta [m^{-1}]$	$M_{cr} [kNm]$	$M_{pl,Rk} [kNm]$	$M_{N,Rk} [kNm]$	$M_u [kNm]$	λ_{LT}	$\chi_{LT,mod}$	$M_{b,Rd} [kNm]$	R_M
0	1499.81	664.0	664.049	693.862	0.665	1.000	664.0	1.04
0.5	1662.86	664.0	657.138	713.818	0.632	0.990	657.1	1.09
0.75	1752.122	664.0	647.564	736.699	0.616	0.975	647.6	1.14
1	1864.2	664.0	637.991	750.500	0.597	0.961	638.0	1.18
1.5	2118.51	664.0	610.382	784.947	0.560	0.919	610.4	1.29
2	2448.68	664.0	578.383	831.789	0.521	0.871	578.4	1.44

Table A4: Numerical and design results concerning the $L=25m$ S355 steel HEB500 beams

$\psi = 1$

$\beta [m^{-1}]$	$M_{cr} [kNm]$	$M_{pl,Rk} [kNm]$	$M_{N,Rk} [kNm]$	$M_{ti} [kNm]$	λ_{LT}	$\chi_{LT,mod}$	$M_{b,Rd} [kNm]$	R_M
0	417.5	1709.8	1709.841	421.0	2.024	0.330	564.2	0.75
0.5	545.5	1709.8	1675.745	597.9	1.770	0.390	666.8	0.90
0.75	625.2	1709.8	1631.599	653.2	1.654	0.420	718.1	0.91
1	717.1	1709.8	1587.452	782.0	1.544	0.470	803.6	0.97
1.5	948.3	1709.8	1472.804	893.6	1.343	0.560	957.5	0.93
2	1269.3	1709.8	1360.176	1293.8	1.161	0.650	1111.4	1.16

$\psi = 0.5$

$\beta [m^{-1}]$	$M_{cr} [kNm]$	$M_{pl,Rk} [kNm]$	$M_{N,Rk} [kNm]$	$M_{ti} [kNm]$	λ_{LT}	$\chi_{LT,mod}$	$M_{b,Rd} [kNm]$	R_M
0	427.7	1709.8	1709.841	454.2	1.999	0.410	701.0	0.65
0.5	561.8	1709.8	1675.745	644.9	1.745	0.520	889.1	0.73
0.75	669.2	1709.8	1631.599	704.6	1.599	0.570	974.6	0.72
1	741.8	1709.8	1587.452	843.6	1.518	0.640	1094.3	0.77
1.5	983.2	1709.8	1472.804	964.0	1.319	0.760	1299.5	0.74
2	1316.1	1709.8	1360.176	1395.6	1.140	0.860	1470.5	0.95

$\psi = 0$

$\beta [m^{-1}]$	$M_{cr} [kNm]$	$M_{pl,Rk} [kNm]$	$M_{N,Rk} [kNm]$	$M_{ti} [kNm]$	λ_{LT}	$\chi_{LT,mod}$	$M_{b,Rd} [kNm]$	R_M
0	1016.5	664.0	664.049	665.1	0.808	0.948	629.2	1.06
0.5	1192.2	664.0	657.138	686.7	0.746	0.985	654.4	1.05
0.75	1314.9	664.0	647.564	706.6	0.711	0.975	647.6	1.09
1	1409.8	664.0	637.991	711.6	0.686	0.961	638.0	1.12
1.5	1683.6	664.0	610.382	767.0	0.628	0.919	610.4	1.26
2	2036.3	664.0	578.383	825.1	0.571	0.871	578.4	1.43

$\psi = -0.5$

$\beta [m^{-1}]$	$M_{cr} [kNm]$	$M_{pl,Rk} [kNm]$	$M_{N,Rk} [kNm]$	$M_{ti} [kNm]$	λ_{LT}	$\chi_{LT,mod}$	$M_{b,Rd} [kNm]$	R_M
0	764.9	1709.8	1709.841	584.4	1.495	0.700	1196.9	0.49
0.5	1111.3	1709.8	1675.745	837.0	1.240	0.830	1419.2	0.59
0.75	1364.2	1709.8	1631.599	942.4	1.120	0.870	1487.6	0.63
1	1529.0	1709.8	1587.452	988.3	1.057	0.930	1590.2	0.62
1.5	2075.4	1709.8	1472.804	1236.4	0.908	0.861	1472.8	0.84
2	2871.1	1709.8	1360.176	1243.4	0.772	0.795	1360.2	0.91

$\psi = -1$

$\beta [m^{-1}]$	$M_{cr} [kNm]$	$M_{pl,Rk} [kNm]$	$M_{N,Rk} [kNm]$	$M_{ti} [kNm]$	λ_{LT}	$\chi_{LT,mod}$	$M_{b,Rd} [kNm]$	R_M
0	1120.7	1709.8	1709.841	616.9	1.235	0.770	1316.6	0.47
0.5	1373.7	1709.8	1675.745	779.3	1.116	0.860	1470.5	0.53
0.75	1490.2	1709.8	1631.599	861.1	1.071	0.910	1556.0	0.55
1	1720.6	1709.8	1587.452	913.9	0.997	0.940	1607.3	0.57
1.5	2217.3	1709.8	1472.804	1058.9	0.878	0.861	1472.8	0.72
2	2975.0	1709.8	1360.176	1162.1	0.758	0.795	1360.2	0.85